TiTaNbHfZr High Entropy Alloy as a Biomedical Coating on Metallic Implant Materials

by

Elif Bedir

A Dissertation Submitted to the
Graduate School of Sciences and Engineering
in Partial Fulfillment of the Requirements for
the Degree of

Master of Science

in

Mechanical Engineering

April, 2019

TiTaNbHfZr High Entropy Alloy as a Biomedical Coating on Metallic Implant Materials

Koç University

Graduate School of Sciences and Engineering

This is to certify that I have examined this copy of a master's thesis by

Elif Bedir

and have found that it is complete and satisfactory in all respects,
and that any and all revisions required by the final
examining committee have been made.

Committee Members:

_____

Assoc. Prof. Demircan Canadinç

_____

Asst. Prof. S. Mine Toker

_____

Asst. Prof. Burak Bal

Date: _____

To my beloved parents,

Oğuz and Cavidan Bedir

ABSTRACT

This study investigates TiTaHfNbZr and $Ti_{1.5}Ta_{0.5}Hf_{0.5}Nb_{0.5}Zr$ high entropy alloy depositions on NiTi shape memory alloy and 316L stainless steel substrates. Nanoindentation, XRD, AFM, SEM, EDS, XPS and ICP-MS analyses were conducted to interpret mechanical properties, microstructures, bioactivities and biocompatibilities of coatings. Study proved that RF Magnetron Sputtering of HEA coatings improve mechanical performance of NiTi SMA and 316L SS substrates, providing better wear resistance. Coatings are much more prosperous to form hydroxyapatite particles than 316L stainless steels, which is an indicator of improved bioactivity. A flawless HEA coating followed by thermal oxidation blocks ion release to surrounding tissue. However, any discontinuities due to erroneously coated films pose a risk of more ion release than uncoated 316L SS. HEA coatings also effective on preventing Ni ion release from NiTi SMAs. This work states that amorphous TiTaHfNbZr and $Ti_{1.5}Ta_{0.5}Hf_{0.5}Nb_{0.5}Zr$ high entropy coating is a promising surface modification for metallic implants.

ÖZETÇE

Bu çalışmada NiTi şekil hafızalı alaşım ve 316L paslanmaz çelik numunelere yapılan TiTaHfNbZr ve $Ti_{1.5}Ta_{0.5}Hf_{0.5}Nb_{0.5}Zr$ yüksek entropili alaşım kaplamaları incelendi. Kaplamaların mekanik özellikleri, mikroyapıları, biyo aktiviteleri ve biyo uyumluluklarının yorumlanabilmesi için nanoiz sertlik testi, XRD, AFM, SEM, EDS, XPS ve ICP-MS analizleri yürütüldü. RF Magnetron Kopartma Yöntemi ile kaplanan yüksek entropili alaşımların NiTi şekil hafızalı alaşım ve 316L paslanmaz çelik numunelerin mekanik özelliklerini iyileştirerek aşınma dayanımlarını artırdığı fark edildi. Kaplamaların, 316L paslanmaz çelik yüzeylerine kıyasla hidroksiapatit partiküllerinin oluşması için çok daha uygun olduğu görüldü. Yüksek entropili alaşım kaplamalarının kaplandıkları yüzeyin biyo aktifliğini artırdığı ispatlandı. Herhangi bir yüzey kusuruna sahip olmayan kaplamaların, termal oksidasyon ile oksitlendiklerinde iyon salınımını yüksek oranda engellediği görüldü. Ancak, kaplama yüzeyindeki herhangi bir çizik, kopuk ya da deliğin, kaplama yapılmamış bir 316L paslanmaz çeliğinden çok daha fazla miktarda Ni iyonu salınımına sebebiyet verdiği gözlendi. Aynı zamanda, kaplamaların NiTi şekil hafızalı alaşımlardan iyon salınmasını engellemekte olduğu yorumlandı. Çalışmada yapılan analizler, TiTaHfNbZr ve $Ti_{1.5}Ta_{0.5}Hf_{0.5}Nb_{0.5}Zr$ yüksek entropili alaşım kaplamalarının metalik implant malzemelerinin biyo performanslarını iyileştirmede yüksek oranda etkili olduğunu ispatladı.

ACKNOWLEDGEMENTS

I would like to express my heartfelt gratitude to my advisor Assoc. Prof. Demircan Canadinç for his guidance throughout my studies. He is an excellent, experienced and principled academician, also an admirable person. He is more than an advisor with his genuine caring for his students. His office was always open whenever I had a problem and with his patience, motivation, kindness and profound knowledge, I was able to overcome any professional and personal obstacles. I sincerely think that every student should come across with an advisor like him in their graduate life.

I also want to express my appreciations to the rest of my thesis jury members, Asst. Prof Mine Toker and Asst. Prof. Burak Bal. Their advices steered my thesis into completion and helped me to manage troubles that I encountered.

I want to thank TÜBİTAK for supporting my MSc. study with the project having project number of 117M826.

I am sincerely thankful to Dr. Amir Motallebzadeh, Dr. Barış Yağcı and Dr. Gülsu Şimşek for their professional contributions to the experimental work of my studies. Their experience and knowledge supplied a solid support to my thesis.

I want to express my deep gratefulness to my dear friends Ahmet Kuzucanlı, Sine İbrahimgil, Hazal Kutluk, Bahar Altunay, Cem Bahadır Aksoy, Tanayça Ünlütürk, Selvi Kaya and Emre Aydoğdu. With their friendship and support, I never felt despair.

My most intensive gratitude goes to my beloved mother and father, Cavidan and Oğuz Bedir for being the light that always leads me to a better future. With their love, trust and support, I became the person who I am now.

TABLE OF CONTENTS

LIST OF TABLES

LIST OF FIGURES

CHAPTER 1. INTRODUCTION

1.1. BIOMATERIALS

The term "biomaterial" was defined by Williams as "a nonviable material used in a medical device, intended to interact with biological systems" in 1987 [1]. Over the decades, scientists and engineers studied biomaterials and their production and processing methods to design artificial body parts, supplementary tools for misfunctioning organs, medical devices and surgical operation tools. Biomaterials to be designed should be safe for the body both chemically and physiologically, they should be biocompatible, their raw materials and production routes should be economic, and they could be processed and utilized easily. Since the beginning of these studies, biomaterials can be grouped into four subsections; metallic materials, ceramics, polymers and composites.

1.1.1. Metallic Biomaterials

Metals are commonly used engineering materials in the production of orthopedics, orthodontics, cardiovascular implants and many surgery equipment. Free electron cloud in metals makes them thermally and electrically conductive. Due to nondirectional bonds, they are also easily deformable. Alloying of the metals brings corrosion and wear resistance, also improves their mechanical properties [1]. Depending on the implant type, required mechanical properties vary. High fatigue strength, corrosion resistance, ductility, wear resistance, high surface roughness and many other properties might be enhanced by certain production methods and treatments. However, biocompatibility is the most important feature. Implant material should not be toxic because implant releases its elements to the body [2]. The most popular bio-metals are stainless steels, cobalt alloys, titanium alloys and NiTi shape memory alloys [3].

Stainless Steels

Steels are alloyed iron with a wide range of alloying elements such as Cr, Ni, Mo, Mn, N and many others. Implant steels are austenitic FCC type since this crystal structure gives them nonmagnetic property which is a crucial requirement for such applications. Alloying element Cr forms a passive oxide layer on the implant body and makes it resistant to corrosion [4]. This layer is mostly composed of Cr_2O_3 but there are other types of oxides too. Ni and Mn are FCC stabilizers, N strengthens the steel and makes it corrosion resistant along with Mo and stabilizes austenite [5,6].

C is added in very small amounts to prevent Cr_3C_2 formation and intergranular corrosion. The most promising stainless steel is 316L and it is generally used for stents and fracture fixation implants. Better mechanical properties and corrosion resistance are achieved by increasing the Mn, Cr and N content of 316L. Rex 734™ is an example of this new alloy. It is necessary to keep Ni content at minimum to avoid nickel poisoning. Mn and N content is increased to compensate the austenite stabilization [2].

Co Alloys

Co alloys have FCC crystal structure and they form a thin layer of chromium oxide. Cr, Ni, Mo and N are alloying elements. N acts as a strengthening element and Ni stabilizes austenitic FCC. CoCrMo is the most common Co alloy in dentistry, hip and knee joint applications. It can be cast to obtain the desired shape. Alloying Co with Cr increases wear resistance and durability. These two mechanical properties of CoCr are even better than Ti and its alloys [7]. Addition of Ni makes Co alloy plastically deformable. Hot forging is needed to shape wrought CoNiCrMo. CoNiCrMo alloys are mostly used as wires, tubings and joints [1,2]. Addition of significant amount of carbon brings wear resistance [8].

Ti Alloys

Ti alloys have three alternative crystal structures: HCP in completely pure Ti (CP Ti) whose symbol is α, HCP mixed with BCC (α+β) in Ti-6Al-4V and Ti-6Al-7Nb and finally BCC (β) in Ti-12Mo-6Zr-2Fe. Composition and processing of the alloy affect these structures. Al and O stabilize α whereas Mo, V and Nb stabilize β. Deformation, cooling rate and heat treatment manipulate the microstructure of β and α+β alloys. Transition

temperature from β to α+β is important in this phenomenon. Ti alloys are also resistant to corrosion owing to the rapid formation of TiO_2 layer. In medical applications research, β alloys are highly popular due to their low Young's modulus, ability to attain large oxygen containments without being brittle, higher notch durability under fatigue and work hardenability. Having low Young's modulus is crucial in protecting the bones in contact with implant from stress shielding. Stress shielding results from stiffness incoherency between the implant and the host bone. Bone softening and implant loosening are the most important results of stress shielding [9]. Since the modulus of conventional implant materials (190 GPa for stainless steel) is greater than that of the bone (17-20 GPa), such problems occur frequently due to stress alteration caused by this difference. Ti-35Nb-4SN β alloy has a Young's modulus in the range of 40 to 60 GPa, which is a significant improvement for medical applications. Ti-35Nb-7Zr-5Ta alloys have higher oxygen content than the other Ti alloys, which is normally undesired because increasing oxygen causes ductility to drop. Contrary to this phenomenon, this specific alloy has both high ductility (≥20%) and high yield strength (1050 MPa). Also, notch sensitivity of α+β alloys is higher than that of β alloys. β alloys also have higher slip systems than α alloys and they are easy to deform and work harden [2]. Ti13Nb13Zr alloy has martensite structure after quenching and subsequent aging, which gives the alloy high corrosion resistance. For bone screws, Ti is an inappropriate choice since its shear strength is low. The interaction mechanisms of Ti alloy surface and the surrounding tissue change with time and the cells, body fluid and implant surface need thorough observation [8]. In general, Ti alloys' mechanical properties are suitable for manipulation and they can be processed according to the desired applications. Along with mechanical properties, improved biocompatibility due to low interfacial energies makes Ti alloys promising biomaterials [10].

NiTi Alloys

NiTi alloys (Nitinol) have distinguishing mechanical properties such as shape memory and superelasticity which make them suitable materials for many applications. Protective oxide layer that is formed due to the oxidation of Ti on the material's surface also provides biocompatibility [11]. Upon heating, shape memory effect converts equiatomic NiTi alloys back to their previously trained shape upon passing through a narrow range of martensite

to austenite transformation temperature. This range is convenient to adjustments with alloying modifications. Shape memory phenomenon is related to thermo-elasticity of diffusionless martensitic phase transformation. Phase transformation can also occur due to plastic deformation. During deformation, twins that are being formed in the structure orient themselves according to the acting principal stresses and this preferred twin variant leads to an overall shape change in the sample. This shape change is not permanent upon heating. When constrained, this behavior becomes beneficial for orthopedic stamps and spinal rods [8]. Along with shape memory effect (SME), NiTi alloys also have super-elasticity property. In this case, austenitic parent phase (B2) transforms into martensite (B19) upon loading and stress remains constant for a certain period, as strain continues to increase. After unloading, no plastic strain remains, and sample turns back to its initial shape before loading. Thanks to SME and super-elasticity, NiTi alloys are generally used in dental, orthopedics and cardiovascular implants. Changing the stoichiometry of the Ni and Ti and production processes makes it possible to change the final properties of the nitinol too [1,12]. Biocompatibility and corrosion resistance of NiTi alloys are proved to be satisfactory *in vivo* tests due to the formation of TiO_2 layer that keeps the surrounding tissue safe from Ni release. This oxide layer is formed with various methods such as sol-gel, anodization and selective oxidation [13-15]. However, brittle oxide layer may have cracks. For extended durations, Ni release from these cracks is likely to be dangerous when it exceeds 9 ppm [16].

1.1.2. Ceramic Biomaterials

Being resistant to compressive loads, having good tribological properties and staying chemically stable inside the body fluids, ceramics have their own share in the implant production [7]. They are also effective reinforcement materials in fiber form because of high strength that they have. They have strong and directional ionic bonds and only a few slip systems. For that reason, they cannot be plastically deformed and shaped and do not show any warning prior to failure. Low ductility and strong resistance to creep in room temperature are also due to the same reason. Their brittleness makes them highly prone to cracks due to stress concentration effect. The existence of microcracks is dangerous under tensile loadings. If they can be eliminated, the resulting product can be ultra-strong

even under tensile stresses. Ceramics also have high hardness and melting temperature. However, they cannot conduct electricity and heat as metals do. For a ceramic to be considered as a suitable biomaterial, it should be nontoxic, noncarcinogenic, biocompatible and bio-functional. Some examples are alumina, zirconia, silicone nitrides and carbons which are known with their inertness [16].

1.1.3. Polymeric Biomaterials

Over many years, polymers have been used as biomaterials due to their biocompatibility, tailorable mechanical properties and optical advantages. Polymers such as PMMA, rubber, silicone and polyurethane were popular in some applications such as bone cement, dental, orthopedics, cardiovascular treatments and plastic surgery. Unfortunately, due to lack of regulations, a lot of earlier products failed due to degradation and cracking. They were not inert enough to body fluids, worn easily and caused inflammation. Due to these problems, silicone plastic surgery implants and Teflon are no more in use. With some improvements, polymeric biomaterials survive in the market until today. Being a biomimetic and an easily manipulated material in terms of mechanical properties like Young's modulus and strength, they can answer both soft and hard tissues' needs. This tailoring is a big advantage over metals and ceramics, and it is possible with arranging the chemistry of the polymer. Ultra-high molecular weight PE is a structural biopolymer, HDPE is used in tendons and expanded PTFE has its place in ligament reconstruction. Expanded PTFE can allow cells to penetrate its structure when it is in the porous form. There are other biopolymers which are biodegradable and one of their most important application is drug delivery. Other application of biopolymers is coating of the surfaces to enhance frictional properties and biocompatibility [1]. Along with these many advantages, sterilization problems come. Since they are not inert to thermal and chemical effects like their opponents, extra precautions and processes are necessary. Some techniques like dry heating, steam sterilization, radiation and chemical sterilization are applicable for different type of polymers under suitable conditions [2].

1.1.4. Composite Biomaterials

A composite material is a combination of two or more different constituents to obtain a superior final product. They are designed in a way that each ingredient supplies a certain property which is desired in the obtained composite material. These ingredients should be greater than atoms, either in micro or macroscale, so an alloy cannot be considered as a composite. For example, bone and wood are natural composites and adobe is synthetic. To produce biomaterials, biocompatible constituents must be used and the interfaces among them must be inert to body fluids. Having at least two constituents makes bio-composites multifunctional. With suitable processing, desired properties such as biocompatibility and biodegradability are achievable [17]. Porous biomaterials are also composite, and they have a unique advantage of tissue penetration. Tooth fillers, PMMA bone cements reinforced with UHMWPE and flexible composite bone plates are some examples for bio-composites. Problems may arise due to water absorption by polymeric matrix such as a decrease in the mechanical properties and swelling. Also, scrap particles generated by the composites may create a foreign matter effect inside the tissue [1].

1.2. WHY METALS?

Being an easily formable, strong, reliable for extended durations and load carrying material, metals have been used in implant and tool production for decades. The first usage of the metals for medical purposes was in dental implants. Metals are used in pure forms such as Ti, Zr, Mg, Zn and as alloys such as stainless steels, Co-Cr alloys, Ti alloys, Zr alloys, Mg alloys and Zn alloys. Their good mechanical properties make them suitable for various applications such as hip and knee joints, cardiovascular stents, dental implants, bone screws and plates. Mg and Zn metals are the common elements in biodegradable metal implant studies [18]. Processes that are used to shape and tailor them to give desired properties are well defined in the industry. Besides their superior mechanical properties that give them a good potential for load-bearing applications, their electrical conductivity also makes them suitable for neuromuscular stimulation implants. Metallic interatomic bonds are responsible for all these advantages over ionically bonded ceramics and covalently bonded polymers. Processing history is also another factor that plays a crucial role on the final properties [1].

1.3. SURFACE MODIFICATION OF METALLIC BIOMATERIALS

After determining the suitable implant material for a specific application, along with bulk materials' properties, surface characteristics of the implant are also of great importance. Scientists and engineers tend to study surface modifications rather than tailoring the whole bulk. This is because surface science can solve many problems using less effort with limited resources. Rigorous processing of the surface is important because the body contacts the implant through its surface and any type of mismatch causes the treatment to fail. For that purpose, chemically or physically coated thin films give them the desired properties. In the case of chemical methods, reactions take place on the surface, and a layer is formed. In physical methods however, sputtering, spraying and evaporation techniques produce the coating. Physical vapor deposition (PVD) is a well-known physical method whereas sol-gel and microarc oxidation are chemical ones.

1.3.1. Physical Vapor Deposition (PVD)

In this process, highly energetic ions or e-beams bombard a target or the target evaporates with the application of high voltages. The vaporized target material then condenses onto the substrate surface. Entire process takes place under vacuum and controlled environment. This method is low cost and applicable for many materials, but the resulting layer is mostly amorphous, and it is hard to control the coating properties [8]. However dense and homogeneous thin layer sticks well onto the flat substrates, even though for the un-flat surfaces some irregularities on the coating are possible. Also, by changing the processing parameters such as temperature and pressure, resultant coating can be manipulated easily, and this enhances the reproducibility [19]. According to *in vivo* tests, biocompatibility and bioactivity of the silicone implants increases with the magnetron sputtering of apatite [20]. PVD process is shown in the Figure 1.1. below [21].

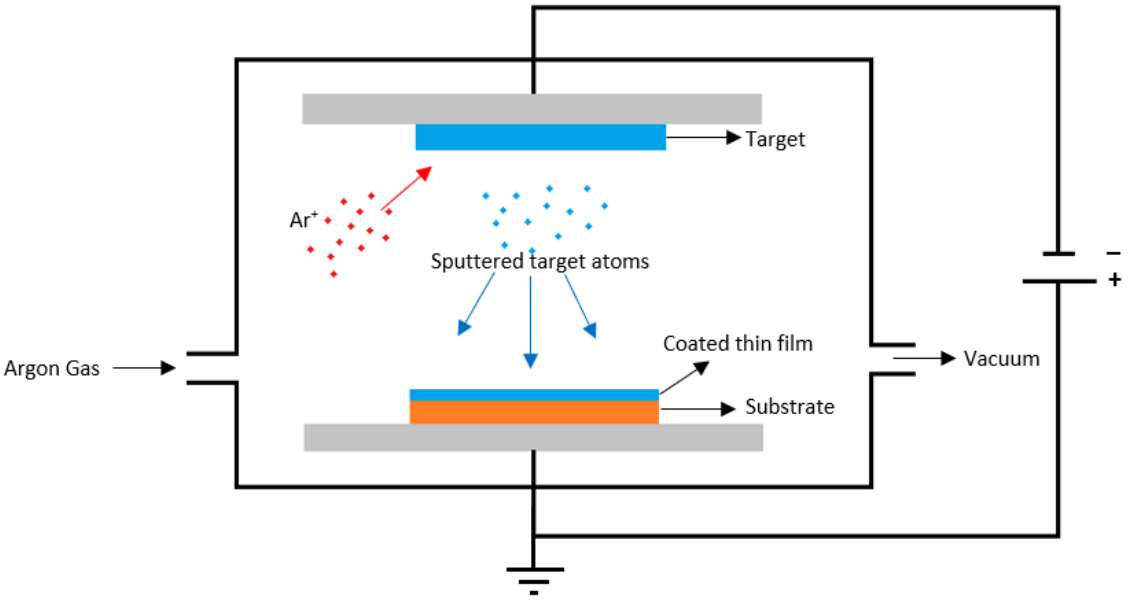

Figure 1.5. Physical vapor deposition [21].

1.3.2. Sol-gel Method

Sol-gel is a perfect method to obtain coatings with well controlled chemical and microstructural properties. Reactants in colloidal suspension are prepared at low temperatures, implants to be coated are then sunk into the suspension generally by dip-coating and dried. With a final baking at very high temperatures for calcination, a highly dense and well-stuck coating forms in the implant surface. Hydroxyapatite and fluorapatite coatings are widely formed via sol-gel method and even some ion additives can be included to enhance cell viability and antibacterial effect. On the contrary to PVD, sol-gel method is effective even in large surface areas and complex surface textures. Coatings can be amorphous and crystalline [20,22]. There are various sol-gel methods other than dip-coating, namely spin coating and electro deposition. They are schematically drawn by Owens et. al. and represented in the Figure 1.2. below [23].

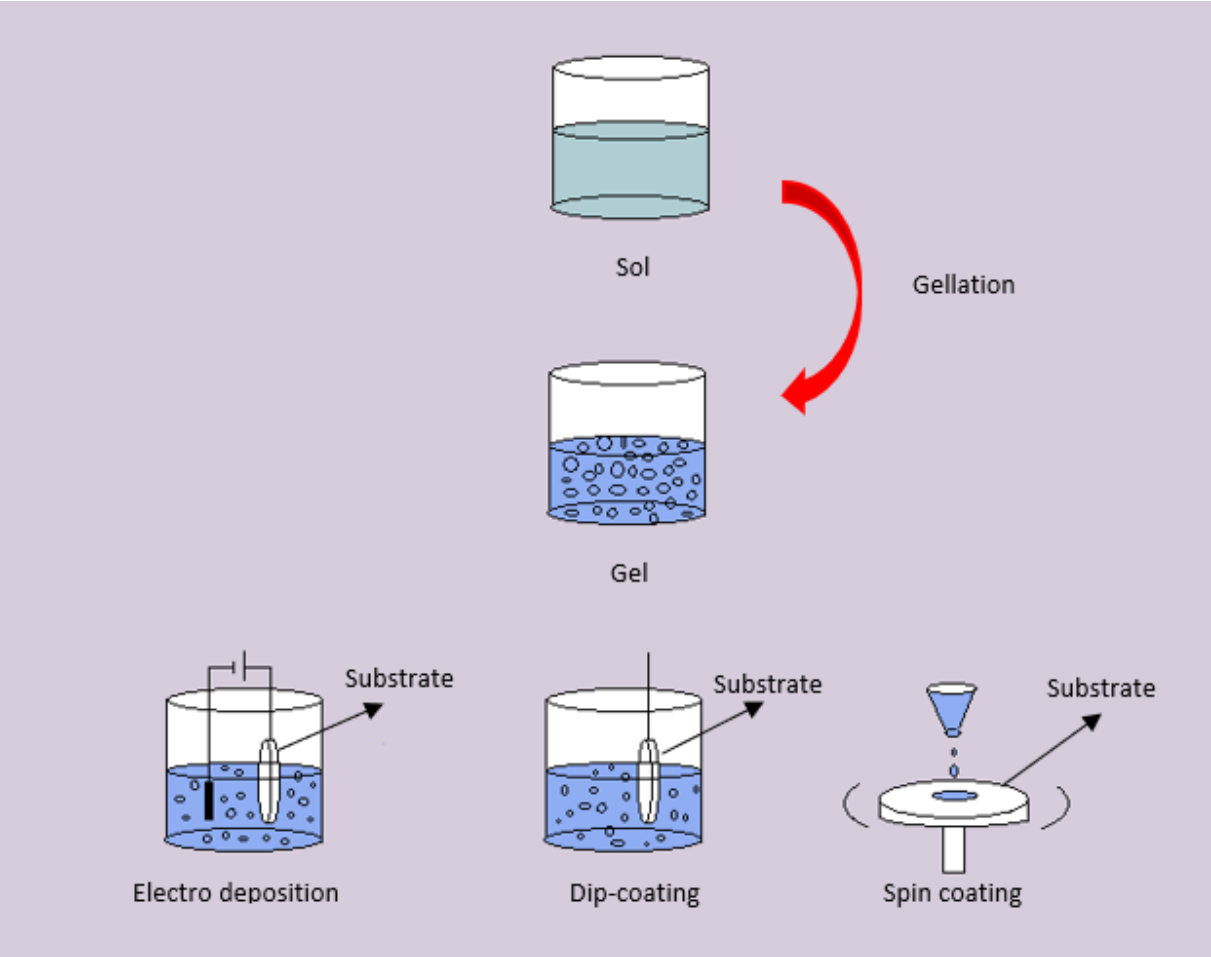

Figure1.6. Different sol-gel methods. Electro deposition, dip-coating and spin coating [23].

1.3.3. Microarc Oxidation

Microarc oxidation (also known as plasma electrolytic oxidation) is an electrochemical process similar to anodization. The only difference is the application of higher potential. Microarc oxidation can be applied on aluminum, magnesium and titanium. In the early stages of the process, an oxide layer is formed. As the voltage increases and exceeds the breakdown potential of the oxide film, electrical discharges take place. These discharges form plasmas and resultant high pressure and temperature cause oxide layer formation. This oxide layer enhances the wear and corrosion resistance of the substrate and the final properties of the layer depends on the electrolyte, substrate composition and the electrical system [24]. A basic sketch of microarc oxidation setup is drawn by Sridhar et. al. is provided in the Figure 1.3. below [25].

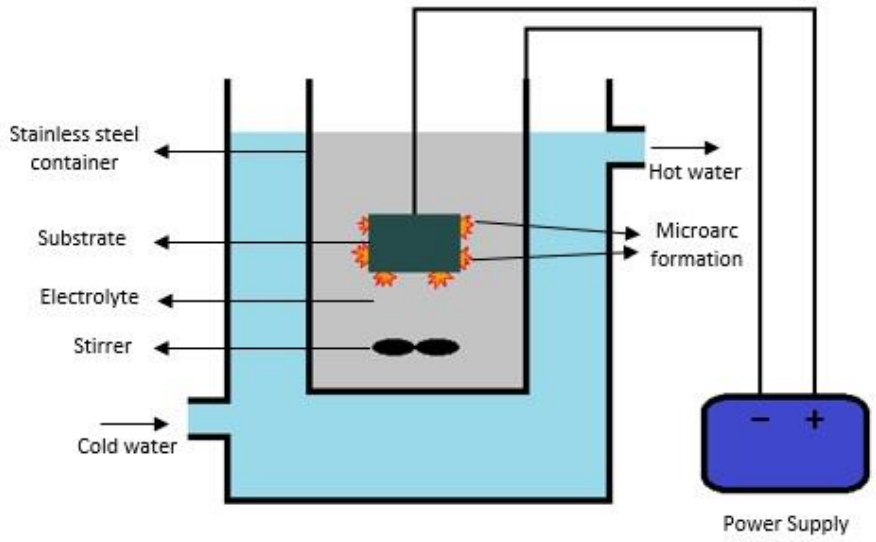

Figure 1. 7. Microarc oxidation technique [25].

1.3.4. Plasma Spraying

Plasma spraying is a method that deposits hydroxyapatite (HA) on the substrates. Ionized gas first melts and then carries the molten HA to the substrate surface. Application of direct current to the H gas mixed with either Ar, He or N ionizes the mixture. Extremely high temperature ionized gas melts and shoots the HA particles towards the surface where they are cooled and stuck. Powder and substrate properties, powder injection parameters and plasma properties are highly effective on the deposition process. For some problems such as oxidation, excessively high pressures and sloppy particle transformation, plasma spraying under vacuum is the solution. Plasma spraying system is depicted in the Figure 1.4. below [26].

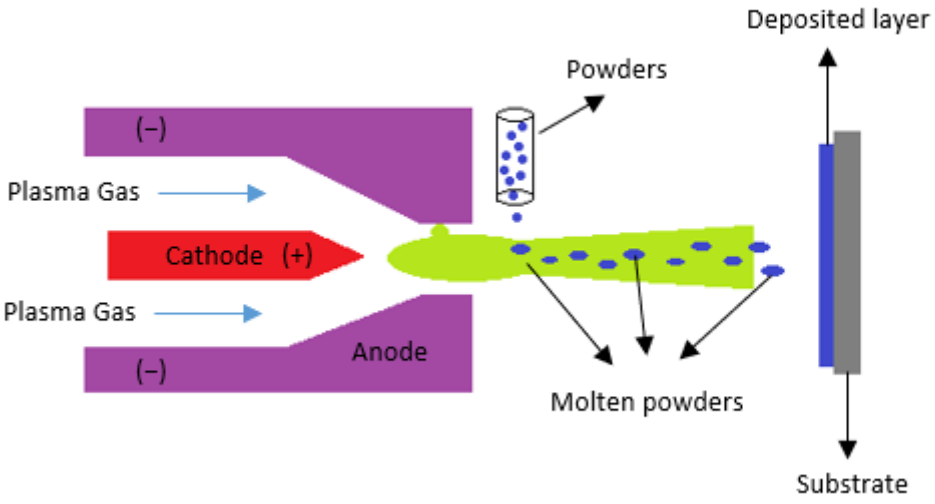

Figure 1.8. Schematic of plasma spraying process [26].

1.3.5. Alkali Treatment

Alkali treatment is held to introduce bone-like apatite layer on the bio-ceramic materials and to increase the bioactivity of Ti and its alloys. In this application, substrates dipped in a 5-10 M NaOH or KOH solution for a certain amount of time, rinsed, cleaned, dried and heat treated at 600-800 ^{0}C at around 105 Torr of pressure. Resultant thin film structure on the Ti surface is a sodium titanate nano-porous hydrogel. Heat treatment increases the amount of crystallized sodium titanate, anatase and rutile titania on the surface. This film enhances the bioactivity of the titanium substrate in the body environment by increasing Ca^{2+} ions and discharges Mg^{2+} ions. Bone-like apatite that is formed after alkali treatment followed by heat treatment makes substrates ready to be attached directly to the bones. Heat treatment is as crucial as the alkali treatment in this [26].

1.3.6. Hydrogen peroxide treatment

Bioactivity of alloyed or pure Ti implants can be increased with the titania gels that are formed on the surface thanks to the H_2O_2 treatment. This titania gels lead to apatite formation when imposed to body environment. Ti-based substrates react with H_2O_2 at 80 ^{0}C for a quite amount of time (up to 72h) and Ti ions are released to the solution as the

reaction continues. At the end of 72 hours, nanopetal structures that formed in the beginning (at the 6th hour) grows so that a film consisting of nanorods appeared on the substrate surface. This film enhances the bioactivity and inhibits the attachment and growth of bacteria on the surface. The titania gel is amorphous when it is freshly formed but can be crystallized with heat treatment and anatase and rutile. Most suitable temperature range for the sake of bioactivity is 400 to 500 ^{0}C thanks to pure anatase phase but higher temperatures introduce rutile phase which drops the bioactivity. Hydrogen peroxide treatment can also be conducted with a $H_2O_2/TaCl_5$ solution followed by a heat treatment under 300 to 600 ^{0}C of temperature [26].

1.3.7. Thermal Oxidation

Thermal oxidation of Ti-based implants is the formation of rutile titania ceramic film formation on the surface by a calcination reaction in regular atmospheric air. Heat treatment oxides the NiTi substrate surfaces by attaching oxygen atoms in the air to the titanium atoms of the substrate. This forms a thin film of passivated titania which acts as a barrier and blocks nickel ion release to the body environment. This enhances bioactivity and biocompatibility of the implant. Once all the Ti atoms spent from the surface, new Ti atoms start to diffuse to the surface from subsurface, leaving a Ni rich region behind. However, the brittle oxide layer causes a risk of Ni ion release which diminishes biocompatibility [26].

1.4. HIGH ENTROPY ALLOYS

High entropy alloys (HEAs) consist of a combination of fully or nearly equiatomic five or more metals. Each component has a share of 5 to 35% atomic percentage in the final mix. High number of different elements increases the mixing entropy, and this forms a stable metallic solid solution. Hence, processing and utilization of HEAs are easy. High configuration entropy that they have does not allow them to form ordered structure or highly restricts it. Solid solutions that they form are in FCC, BCC or HCP system. Highly distorted lattice structure that these alloys have make them strong. Other than promising mechanical properties, their structure brings unique properties such as diffusion barrier

effect, enhanced electrical and thermal properties. Current studies also involve biomedical purposes. Thanks to these studies, antibacterial and hydrophilic properties are achievable. Diffusion barrier property of HEAs can be used as a protection against toxic and inflammatory effects of biomaterials that are currently in use. Their wear resistance and strength make them suitable to load-bearing applications [27].

Throughout the history of metallurgy, it is understood that using alloyed metallic materials instead of pure metals provides many properties and functions to the final product. For that purpose, conventional alloys having only one principal element mixed with various alloying elements are produced using certain processes. Along with conventional alloys, other metallic materials such as intermetallics, metallic glasses and quasicrystals are synthesized and being used in different industries.

In the second half of the eighteenth century, design of a new concept which is called high entropy alloys (HEAs) began with the studies of German scientist Frans Karl Achard. On the contrary to the existing alloy systems that have single principal element/compound, he used five to seven multi-principal elements [28]. By alloying plenty of elements such as Fe, Cu, Sn, Pb, Zn, Bi, Sb, As, Ag, Co and Pt, he managed to study more than 900 different alloy systems. Upon his studies he conducted mechanical and corrosion tests.

By definition, HEAs are composed of five equiatomic or near equiatomic elements but using more than five elements is also possible. Atomic percentage of each element ranges between 5% and 35% [29]. HEAs maintain their stability even under high temperatures for their solid solution phases have high entropy of mixing. Stability is a crucial requirement for an easily manufactured and tailorable material. The more equiatomic the alloy, the stable it gets because mixing entropy is favored by equal atomic percentages. Minor alloying elements can also be added to modify the structure and the characteristics of the alloy. For an element to be considered as a minor alloying element, it should have less atomic percentage than 5%. Hence there are countless different combinations of metallic elements and their atomic percentages, synthesis of a great number of HEAs is possible.

HEAs have a smaller number of phases than Gibbs phase rule states under equilibrium conditions as Cantor et al. declared. This trend is also valid for non-equilibrium cases and the main reason for such a behavior is the high mixing entropy of the alloys. High mixing

entropy promotes intersolubility of the components of the alloy system. Also, the multi-principal element nature of the system kinetically restricts the diffusion of atoms and prevents new phases to form. As the number of elements that involved in the system increases, entropy of mixing (configurational entropy) increases and this changes phase formation and kinetics. Not only entropy, but also enthalpy of mixing and the atomic radii of the constituent elements affect the phase formation. Resultant phases manipulate material characteristics and properties [29,30]. In fact, there are four main phenomena that play the most important roles in defining properties of HEAs. They are namely high entropy, severe lattice distortion, sluggish diffusion, and cocktail effects [31].

1.4.1. High Entropy Effect

High entropy of mixing reduces the number of phases by promoting solid solution formation. Obtaining solid solutions is the most effective way in diminishing the overall Gibbs Free Energy of the system by following the following formula:

$$\Delta G_{mix} = \Delta H_{mix} - T\Delta S_{mix}$$

Thermodynamically, stability is satisfied when the smallest ΔG_{mix} is achieved. Thus, solid solutions are preferred as the main phase of HEAs. This means, less complicated microstructures are obtained by overcoming the formation of many different phases, intermetallics and other segregated phases. Otherwise, resulting alloy would be brittle. High entropy also provides improved corrosion resistance since it decreases the overall free energy of the system [27].

1.4.2. Severe Lattice Distortion Effect

Since HEAs are composed of different elements, each atom in the structure has neighboring atoms of various elements. Every atom in the HEA lattice has different atomic radius and this leads to strain and stress on the system [32,33]. In addition, the bonds in between the atoms have different energies and together with stress and strain, asymmetry and distortion take place in the lattice. An alloy with a distorted lattice gains certain properties such as hardness and strength but loses thermal dependency on its

characteristics. Electrical and thermal conductivities of HEAs are affected inversely with the lattice distortion due to electron and phonon scattering [27,34]. Due to the distortion, scattering takes place during XRD analyses and peak intensities drop [32].

1.4.3. Sluggish Diffusion Effect

Since HEAs are solid solutions of many different elements, atomic diffusion in their matrices takes place in a special way. Due to varying kinds of atoms in the lattice, each site has a different lattice potential energy. This different LPE causes diffusion hindering and higher activation energy as Tsai et al. states [33]. Sluggish diffusion is mainly due to barrier effect of low LPE regions in the lattice. Hence the nucleation and growth of new phases requires diffusion, microstructure and final properties of HEAs are directly affected by sluggish diffusion. Sluggish diffusion controls precipitation formation, recrystallization and grain growth mechanisms in such a way that it improves toughness, strength and creep resistance of the alloy [27].

1.4.4. Cocktail Effect

HEAs contain five or more alloying elements and each element provides characteristic contributions the final properties of the alloy. Along with the phase numbers and morphologies, properties of the resulting phases also affect the alloy. Constituent phases can be regarded as separate solid solutions that being affected by their own elements' properties and elemental interactions. Cocktail effect widens the properties that anticipated by mixture rule by atomic scale interactions between dissimilar atoms [35].

To conclude the above-mentioned four effects, following summary can be made. High entropy effect enables the formation of simpler phases, sluggish diffusion effect hinders the kinetics of phase transformations and finally lattice distortion and cocktail effects manipulate the alloy's properties.

1.4.5. Synthesis and Processing

HEAs are produced in bulk and coating forms. Casting and powder metallurgy are used for bulk alloy production and deposition method is used for coated HEAs.

Casting Method

Vacuum arc melting, vacuum induction melting and melt spinning are the main casting routes. However, arc melting is the most preferred production route since it enables the melting of most of the metals by reaching very high temperatures. But in that case, some precautions must be taken to overcome loss of the low melting point elements. Induction heating furnaces could be used, or the initial material batch could be prepared in accordance with the evaporation of some metals. Dendritic solidification takes place during casting of the HEAs with this method. It is important to have a homogeneous structure throughout the alloy. Cooling and solidification rates must be controlled studiously.

Powder Metallurgy Method

Basically, in this technology, powder forms of the alloying elements are alloyed mechanically to obtain a homogeneous structure and then sintered together. Mechanical alloying takes place inside a high-energy ball milling machine and fractured metallic powders are welded together as diffusion takes place. Final structure is an equiatomic nanocrystallized or amorphous nanoparticle [36,37]. Subsequent sintering is applied for densification. To overcome the risk of grain growth, spark plasma sintering is generally preferred.

Deposition Method

Deposition can be made using both liquid and vapor phase precursors. The mostly used deposition techniques for vapor phase are magnetron sputtering and plasma nitriding.

Various substrates can be coated with HEAs to advance the surface properties like corrosion and wear resistance. In sputtering, a solid target which is made of the HEA to be coated on the substrate is exposed to charged inert gas ions. Cut off atoms of the target is then collected on the substrate surface with the help of DC bias or radio frequency (RF). Deposition thickness is generally smaller than 1 μm but can be controlled with the adjustments that are made on the power, voltage and inert gas pressure [38]. With the application of DC magnetron sputtering, amorphous HEA film is acquired according to study of Chang et al. [39]. Even if it is rarely preferred, plasma nitriding can replace magnetron sputtering for 50-100μm thick nitrided coatings [27]. Nitriding provides better wear resistance [40]. For the liquid phase HEA precursor however, cladding is used. Cladding is similar to welding and with the help of tungsten inert gas (TIG) or laser, two different methods are applicable for the HEA coating on the substrates. Cladding material is the powder mixture of the HEA elements to be coated on the surface. Resulting cladded HEA layer improves the wear resistance of the substrate [41].

1.4.6. Mechanical Properties

The most crucial advantage of HEAs over conventional alloys are their superior mechanical properties. Their hardness, strength, fracture toughness and fatigue resistance are highly promising for many engineering applications. Principal and minor alloying elements together with production paths have important role on the final properties of the alloys.

Hardness

Hardness values of HEAs vary in the range between 140 HV to 900 HV. Lattice distortion contributes to the hardening of the alloy because it causes solution hardening. Increasing the number of elements up to a certain point also improves the hardness. Especially, the existence of Al and Ti elements in the composition have hardening effect. Al is a special element since it forms strong bonds with neighboring atoms, it distorts the lattice with its large volume and it is a BCC forming element. BCC is a harder and stronger phase compared to FCC, but it brings brittleness to the alloy. So, it is observed that FCC

structured HEAs that are produced without any heat treatment application have low hardness values [5,42,43]. There are other possible elements with large radii that have the chance of forming secondary phases to contribute to the hardening and strengthening. Upon the annealing treatment of HEAs, age hardening takes place. Hardening behavior with the aging varies from one alloy to another. In this heat treatment, hardness of the alloy increases with the precipitations that are formed, but grain growth must be controlled thoroughly to overcome softening. Work hardening is also possible for HEAs.

Compressive Behavior

Many different testing and production conditions of the alloy affect the mechanical analysis of HEA samples. Considering the loading temperature, strain rates, alloying elements, heat treatment applications, and microstructure of the alloy upon testing is highly important for the design of an alloy for a certain application. For example, Cu ingredient gives brittleness to the alloy under compression. Even if the yield strength tends to decrease with temperature, elements that are used specifically for the refractory applications increases the mechanical properties at elevated temperatures. Fractography analyses showed that crack formation and shearing take place at low temperatures but as the temperature rises, GB sliding and void formation start. The sample geometry is also important hence it changes the cooling rate upon production steps. Slowly cooled parts have low strength and less plasticity [44].

Tensile Behavior

As the nature of production methods enforce, HEA structures have casting defects such as shrinkages and micropores. The most efficient way to investigate the effects of these defects on the mechanical properties is via tensile testing. Results showed that HEAs have promising tensile properties. FCC HEAs resemble ductile materials with rather low strengths. BCC and FCC mixed structure HEAs show a sudden improvement on their strength but their ductility is sacrificed. Purely BCC HEAs are highly brittle. Grain size affects the strength as in conventional alloys, grain coarsening drops strength of the alloy. Stress-strain diagrams of HEAs differ around yielding point. Coarse grained alloys do not

show a well-defined yielding region in their curves whereas fine grained ones do. After yielding, load drops slightly in the small grained HEAs. Serrations can be seen regardless of the grain size [42]. Since numerous different HEAs can be synthesized using limitless possible combinations of many elements and compositions, yield strength and ductility measurements of HEAs lie in a very vast range. HEAs can be fractured in brittle, ductile or mixed manner. This behavior is affected by the elements that are used in the alloying. Increasing temperature favors ductile fracture.

Fatigue Behavior

In the structure of every material, there are certain regions which are prone to fatigue. These regions are mainly microcracks, microvoids, casting defects and oxide particles. Since there is stress concentration on these sites, fatigue mechanisms start and fatigue life of the alloy decreases. Stress concentration can also be effective on other regions due to the geometry of the product. Despite the above-mentioned defects restricts the fatigue resistance, it is certainly possible to synthesize HEAs that can overcome the fatigue properties of conventional alloys, superalloys and bulk metallic glasses [42].

1.5. MOTIVATION

In the earlier studies that aimed to develop bioactive and biocompatible surfaces, ceramic coatings are generally offered. However, even if they are biocompatible, there is a mismatch between the mechanical properties of coating and the substrate. This inevitably leads to crack formation and propagation which results in Ni release. So, in the current study, metallic coating is proposed as a more profitable alternative. There are some specifications for the coating such as bioactivity, durability, satisfying mechanical properties, good adhesion behavior and effective protection against toxic and allergic effects. In this study, TiTaNbHfZr high entropy alloy is used as a coating material for 316L stainless steel and NiTi substrates. For coating, PVD method is applied by using RF Magnetron Sputtering. After the substrates are coated, XRD, SEM-EDS and AFM analyses are conducted for microstructural characterization and nano-indentation test for the mechanical property characterization. For the bioactivity measurements, SBF immersion

tests are conducted and the resulting hydroxyapatite nucleation is observed via SEM analysis. Ni and Cr release to the immersion fluid is also measured by using ICP-MS to evaluate the biocompatibility of the HEA coating.

Bibliography

1. Wong, J. Y. & Bronzino, J. D. *Biomaterials*. (Taylor & Francis Group, LLC, 2007).
2. Ducheyne, P. (Ed.), *Comprehensive Biomaterials*. (Elsevier, 2011).
3. Zhou, Z. *et al.* Development of Co-based bulk metallic glasses as potential biomaterials. *Mater. Sci. Eng. C* **69,** 46–51 (2016).
4. Bait, L., Azzouz, L., Madaoui, N. & Saoula, N. Influence of substrate bias voltage on the properties of TiO2 deposited by radio-frequency magnetron sputtering on 304L for biomaterials applications. *Appl. Surf. Sci.* **395,** 72–77 (2017).
5. Yu, P. F. *et al.* Nanotwin' s formation and growth in an AlCoCuFeNi high-entropy alloy. *Scr. Mater.* **114,** 31–34 (2016).
6. Ren, B. *et al.* Effect of elemental interaction on microstructure of CuCrFeNiMn high entropy alloy system. *J. Alloys Compd.* **493,** 148–153 (2010).
7. Chu, P. K., Chen, J. Y., Wang, L. P. & Huang, N. Plasma-surface modification of biomaterials. *Mater. Sci. Eng. R Reports* **36,** 143–206 (2002).
8. Pilliar, R. M. in *Biomedical Materials* 41–81 (2009).
9. Elahinia, M. H., Hashemi, M., Tabesh, M. & Bhaduri, S. B. Manufacturing and processing of NiTi implants: A review. *Prog. Mater. Sci.* **57,** 911–946 (2012).
10. Ponsonnet, L., Reybier, K., Jaffrezic, N., Comte, V. & Lagneau, C. Relationship between surface properties (roughness , wettability) of titanium and titanium alloys and cell behaviour. **23,** 551–560 (2003).
11. Tian, H., Schryvers, D., Liu, D., Jiang, Q. & Van Humbeeck, J. Stability of Ni in nitinol oxide surfaces. *Acta Biomater.* **7,** 892–899 (2011).
12. Yoneyama, T & Shuichi Miyazaki, S. (Eds.) *Shape memory alloys for biomedical applications. (Woodhead Publishing Limited, Cambridge,2009).*
13. Aun, D. P. *et al.* Development of a flexible nanocomposite TiO2 film as a protective coating for bioapplications of superelastic NiTi alloys. *Appl. Surf. Sci.* **375,** 42–49 (2016).
14. Bayat, N., Sanjabi, S. & Barber, Z. H. Improvement of corrosion resistance of NiTi sputtered thin films by anodization. *Appl. Surf. Sci.* **257,** 8493–8499 (2011).
15. Neelakantan, L., Swaminathan, S., Spiegel, M., Eggeler, G. & Walter, A. Selective surface oxidation and nitridation of NiTi shape memory alloys by reduction annealing. *Corros. Sci.* **51,** 635–641 (2009).
16. Tan, L., Dodd, R. A. & Crone, W. C. Corrosion and wear-corrosion behavior of NiTi modified by plasma source ion implantation. *Biomaterials* **24,** 3931–3939 (2003).
17. Kumar, S. S. D., Rajendran, N. K., Houreld, N. N. & Abrahamse, H. Recent Advances on Silver Nanoparticle and Biopolymer Based Biomaterials for Wound Healing Applications. *Int. J. Biol. Macromol.* #pagerange# (2018). doi:10.1016/j.ijbiomac.2018.04.003

18. Li, H. F. & Zheng, Y. F. Recent advances in bulk metallic glasses for biomedical applications. *Acta Biomater.* **6,** 2740–2750 (2016).

19. Daviðsdóttir, S. *et al.* Investigation of DC magnetron-sputtered TiO 2 coatings : Effect of coating thickness, structure, and morphology on photocatalytic activity. *Appl. Surf. Sci.* **313,** 677–686 (2014).

20. Nouri, A. & Wen, C. *Surface coating and modi fi cation for metallic biomaterials*. *Surface Coating and Modification of Metallic Biomaterials* (2015). doi:10.1016/B978-1-78242-303-4.00001-6

21. Pampuri, S., Johnston, A. B., Jian Wan, O'Hara, P. G. & McLoone, S. On Regression Methods for Virtual Metrology in Semiconductor Manufacturing. in 380–385 (2014). doi:10.1049/cp.2014.0718

22. Krysa, J. *et al.* TiO2 and Fe2O3 Films for Photoelectrochemical Water Splitting. *Molecules* **20,** 1046–1058 (2015).

23. Owens, G. J. *et al.* Sol–gel based materials for biomedical applications. *Prog. Mater. Sci.* **77,** 1–79 (2016).

24. Erfanifar, E., Aliofkhazraei, M., Nabavi, H. F. & Rouhaghdam, A. S. Growth kinetics and morphology of microarc oxidation coating on titanium. *Surf. Coat. Technol.* **315,** 567–576 (2017).

25. Sridhar, S., Viswanathan, A., Venkateswarlu, K., Rameshbabu, N. & Parthasarathi, N. L. Enhanced visible light photocatalytic activity of P-block elements (C, N and F) doped porous TiO2coatings on Cp-Ti by micro-arc oxidation. *J. Porous Mater.* **22,** 545–557 (2015).

26. Driver, M. (Ed), *Coatings for biomedical applications* (Woodhead Publishing Limited, Cambridge, 2012).

27. Murty, B. S., Yeh, J. W. & Ranganathan, S. High Entropy Alloys. *High Entropy Alloy.* 159–169 (2014). doi:10.1016/B978-0-12-800251-3.00010-9

28. Cavaliere, P. *Spark Plasma Sintering of Materials*. *Spark Plasma Sintering of Materials* (2019). doi:10.1007/978-3-030-05327-7

29. Yeh, J.W., Chen, S.K., Lin, S.J., Gan, J.Y., Chin, T.S., Shun, T.T., et al., (2004). Nanostructured high-entropy alloys with multiple principal elements: novel alloy design concepts and outcomes. Adv. Eng. Mater. 6, 299303.

30. Cantor, B., Chang, I.T.H., Knight, P., Vincent, A.J.B., (2004). Microstructural development in equiatomic multicomponent alloys. Mater. Sci. Eng. A 375377, 213218.

31. Yeh, J.W., (2013). Alloy design strategies and future trends in high-entropy alloys. J. Met. 65,17591771.

32. Yeh, J.W., Chang, S.Y., Hong, Y.D., Chen, S.K., Lin, S.J., (2007). Anomalous decrease in X-ray diffraction intensities of CuaNiaAlaCoaCraFeaSi alloy systems with multi-principal elements. Mater. Chem. Phys. 103, 4146.

33. Tsai, K.Y., Tsai, M.H., Yeh, J.W., (2013). Sluggish diffusion in CoaCraFeaMnaNi highentropy alloys. Acta Mater. 61, 48874897.

34. Kao, Y.F., Chen, S.K., Chen, T.J., Chu, P.C., Yeh, J.W., Lin, S.J., (2011). Electrical, magnetic and Hall properties of AlxCoCrFeNi high-entropy alloys. J. Alloys Compd. 509, 16071614.

35. Ranganathan, S., (2003). Alloyed pleasures: multimetallic cocktails. Curr. Sci. 85, 14041406.

36. Benjamin, J.S., (1970). Dispersion strengthened superalloys by mechanical alloying. Metall. Mater. Trans. B 1, 29432944.

37. Fecht, H.J., Han, G., Fu, Z., Johnson, W.L., (1990). Metastable phase formation in the ZraAl binary system induced by mechanical alloying. J. Appl. Phys. 67, 17441748.

38. Chen, H.C., Jan, D.J., Chen, C.H., Huang, K.T., (2013). Bond and electrochromic properties of WO3 films deposited with horizontal DC, pulsed DC, and RF sputtering. Electrochim. Acta 93, 307313.

39. Chang, H.W., Huang, P.K., Davison, A., Yeh, J.W., Tsau, C.H., Yang, C.C., (2008). Nitride films deposited from an equimolar AlaCraMoaSiaTi alloy target by reactive direct current magnetron sputtering. Thin Solid Films 516, 64026408.

40. Tang, W.Y., Chuang, M.H., Lin, S.J., Yeh, J.W., (2012). Microstructures and mechanical performance of plasma-nitrided Al0.3CrFe1.5MnNi0.5 high-entropy alloys. Metall. Mater. Trans. A 43, 23902400.

41. Chen, J.H., Hua, P.H., Chen, P.N., Chang, C.M., Chen, M.C., Wu, W., (2008). Characteristics of multi-element alloy cladding produced by TIG process. Mater. Lett. 62, 24902492.

42. Zhang, Y., Gao, M. C., Yeh, J. W., Liaw, P. K. (2016). High-Entropy alloys: fundamentals and applications.

43. Lin C-M, Tsai H-L, Bor H-Y (2010) Effect of aging treatment on microstructure and properties of high-entropy Cu0.5CoCrFeNi alloy. Intermetallics 18(6):1244–1250. doi:10.1016/j.intermet.2010.03.030

44. Wang FJ, Zhang Y, Chen GL, Davies HA (2009) Cooling rate and size effect on the microstructure and mechanical properties of AlCoCrFeNi high entropy alloy. J Eng Mater Technol 131(3):034501. doi:10.1115/1.3120387

CHAPTER 2. EXPERIMENTAL PROCEDURE

In the sample preparation and through examination procedure of this study, some devices and analysis methods were used. Sample preparation starts with the production of the 316L stainless steel, NiTi alloy and HEA substrates. TiTaHfNbZr HEAs were cast with arc melting as discussed before. These HEAs were used as substrates and as PVD targets. EDM was used to cut substrates and it was followed with grinding and polishing to provide suitable surfaces for HEA coating. HEA coatings with different thicknesses were deposited on 316L stainless steel, NiTi and silicon (100) substrates with PVD. After the samples were produced, microstructures, mechanical properties and bioactivities of the samples were examined. For microstructural analyses, SEM, EDS, XRD and AFM were used. Mechanical properties -namely hardness and elastic modulus- were measured in a nanoindentation test machine. For bioactivity and biocompatibility tests, samples were immersed in SBF (blood) for various durations and their surfaces and immersion fluids were analyzed in SEM&EDS and ICP-MS respectively.

2.1. SAMPLE PREPARATION

2.1.1. Electrical Discharge Machining (EDM)

EDM is a machining technique which uses a spark generated between the cutter electrode and the workpiece to remove material from surface. A dielectric fluid hosts the electrical field between the electrode and the material to be cut. It supplies a suitable environment for a stable spark and washes away the removed material. Due to its working mechanism, EDM can only be used to machine conductive materials [1]. Since EDM does not apply a huge amount of force or pressure to the part, it causes a small amount of destruction on the sample comparing to other machining tools. Since it uses only the spark (but not force) to cut the workpiece, even high strength materials can be machined easily. Also, during machining cutter electrode and the cutting sample do not get in contact directly. Only a fine spark removes material. So, EDM can work with very small samples in close tolerances and high precision. Any desired final geometry is possible. However, EDM is not suitable for mass production since it is not a quick process. Also, surface quality is sometimes low and due to cutter electrode wear, desired geometry is not always obtained.

Heat generation due to the spark causes residual stresses and heat affected zones (HAZ) [2,3]. However, for this study only a limited number of samples is needed, so electrode wear is not a problem. Flashes and surface roughness due to cutting can easily be removed with grinding. Also, samples are so small that any other method would damage them. With EDM, disc shaped, square and rectangular samples were cut. 316L substrates were cut as discs having 10 mm diameter and 1 mm thickness. NiTi substrates are in 10 mm x 10 mm x 2 mm sizes. Bulk HEA samples are cut in rectangular shapes having 10 mm x 5 mm x 1 mm.

2.1.2. Grinding & Polishing

Grinding is a process which is held to get rid of surface roughness of samples. Abrasive particles such as alumina, zirconia and silicon carbide are coated on a paper fixed on a rotating disk. Material to be grinded is kept in contact with this rotating abrasive paper. Water is dripped onto the paper to prevent excessive heating and to wash grinded particles off. With grinding, shiny surfaces can be obtained even from very rough surfaces. Polishing follows grinding to provide further smoothing. This process is very similar to grinding but instead of abrasive paper, alumina slurry is poured on a fabric coated rotating disk to remove material. This slurry polishes the surface with abrasive alumina particles. In the grinding and polishing of the samples, 120 to 2000 grit SiC emery papers and 30 μm alumina slurry were used. It also acts as coolant and carries removed material away. After grinding and polishing is completed, samples were cleaned using ultrasonic cleaner respectively with ethanol, acetone and distilled water and dried. Surfaces are smooth and clean enough to be PVD coated. Figure 2.1. below shows the grinding and polishing machine.

Figure 2.1. Metallographic lapping and polishing machine.

2.1.3. PVD Coating

Principal working mechanism of physical vapor deposition method was already introduced in the Chapter 1. Considering the mentioned superiorities of PVD compared to its alternatives, samples were PVD coated in this study. Among different PVD techniques such as DC sputtering, ion beam sputtering and RF magnetron sputtering, latter was used. Even though RF sputtering is advantageous since it can be used to coat insulators, this phenomenon is irrelevant in this study because all substrates are metallic materials. However, plasma density in RF magnetron sputtering is rather high due to the high frequency power supply. This provides faster coating which is highly desirable for this study [4]. A Nanovak NVTS-400 PVD machine was used with no substrate bias. Ar was used as inert gas and its flow was 10 SCCM. Chamber base pressure was below $1x10^{-3}$ Pa and coating took place at room temperature with a sputtering power of 100 W. Three different HEA targets were used. They were casted as discs with 50.8 mm diameter and 6.3 mm thickness. Prior to HEA coating, substrate surfaces were bombarded with Ar plasma for 10 minutes with a power of 80 W for cleaning. Silica wafers and NiTi alloys were coated with 750 nm and 1500 nm thick TiTaHfNbZr HEA films. 316 L stainless steels were coated with thick 1000 nm TiTaHfNbZr and $Ti_{1.5}Ta_{0.5}Hf_{0.5}Nb_{0.5}Zr$ HEA films. After the films were coated, some of the 316 L stainless steels were thermally oxidized at 300 C° for 5 minutes in air atmosphere. Figure 2.2. below shows the Nanovak NVTS-400 PVD machine.

Figure 2.2. Nanovak NVTS-400 PVD machine.

2.2. MICROSTRUCTURAL ANALYSIS

2.2.1. Scanning Electron Microscopy

Scanning electron microscopy (SEM) uses a focused electron beam so that it can collect the surface topography data of the samples. Thanks to high energy of this electron beam, details that are invisible in optical microscopy can be investigated. Electrons are sent towards the sample's surface via an electron gun and condensed into one focused beam with condenser lenses. When this beam hits the surface, the interaction of the sent electrons with surface atoms causes emissions. Back-scattered electrons, secondary electrons and X-rays are emitted depending on the depth of interacting surface atoms. These emitted electrons and X-rays are collected with special detectors and converted to surface morphology data using computer programs. A simple scheme of a SEM device and emissions from the surface is given in the Figure 2.3. and Figure 2.4. below [5,6].

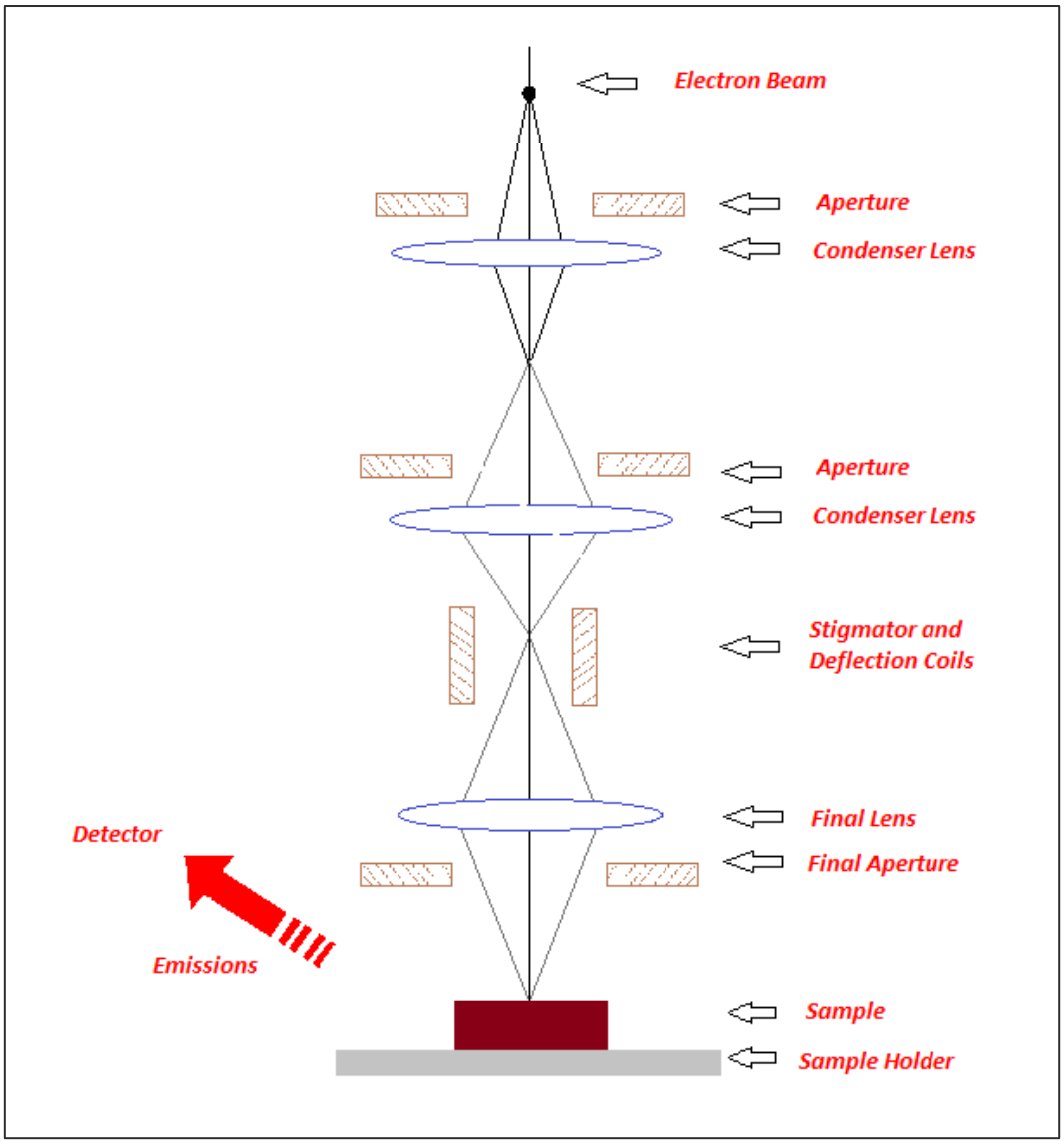

Figure 2.3. Representative sketch of a SEM device [5].

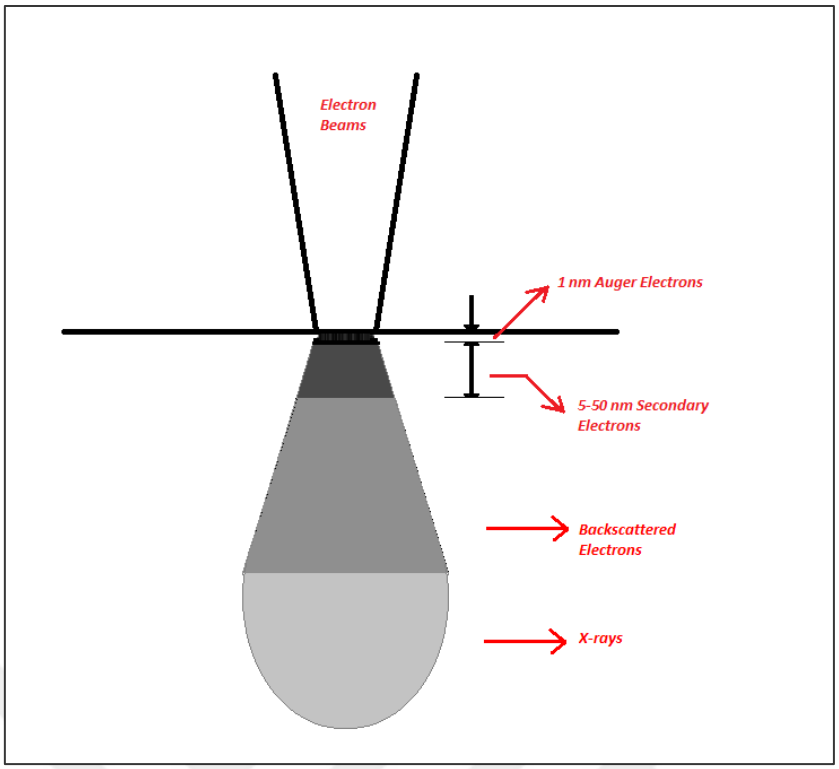

Figure 2.4. Emitted electrons and X-rays from the sample's surface [6].

A ZEISS Ultra Plus and Zeiss Evo LS15 SEM devices were used in this study. Morphologies of HEA coatings on NiTi alloys and 316 L stainless steels were investigated from top view. Since the samples are all conductive, no extra conductive coatings were applied. Bulk HEAs were also investigated. In addition to top view, cross-sectional SEM images of HEA coatings on silica wafers were also taken to examine the coating uniformity throughout the surface. Using silica instead of NiTi or stainless steel samples was preferred for the sake of easiness and it does not cause any difference in the cross-sectional view of the film. In the Figure 2.5., Zeiss Evo LS15 and Zeiss Ultra Plus Scanning Electron Microscopes which are used in the analyses are given.

(a) **(b)**

Figure 2.5. (a) Zeiss Evo LS15, (b) Zeiss Ultra Plus Scanning Electron Microscopes.

2.2.2. Energy-Dispersive X-Ray Spectrometry

Energy dispersive X-Ray Spectrometry (EDS) is an auxiliary tool of SEM which provides chemical information of the test sample. It analyzes the X-rays emitted from the sample, compares the energy and quantity information of them with its library of elements and finds the elemental ingredient of sample [7]. EDS can be performed on a certain point or through a horizontal or vertical line on the sample's surface. By that, it can draw elemental line and depth profiles, it can also draw a map of the surface indicating all the constituent elements. In this study, EDS was used to detect hydroxyapatites formed on the immersion samples and to examine the coating by drawing concentration depth profiles.

2.2.3. X-ray Diffraction

X-ray Diffraction provides information on a crystalline material's molecular structure, phase structure, crystallinity and morphology. Working principle of X-ray diffraction (XRD) is related to Bragg's law $n\lambda = 2d \sin\theta$. In this law, d is the distance between planes of lattice structure, λ is the wavelength of sent X-ray, n is the reflection order and 2θ is the scattered X-ray's angle. During XRD, X-rays are sent to the sample's surface collide with the nuclei of the sample's atoms. Since nuclei are heavy structures, they diffract the X-ray. By measuring the diffraction angles and scattering intensities, crystallinities of the

samples can be investigated [8]. In this study, HEA films and bulk HEAs were analyzed with a GIXRD-Bruker D8 Advanced device. Grazing incidence was used because the film thicknesses are no more than 1500 nm and X-ray beam needs to be sent almost parallel to the surface. To do that, a Cu K_α radiation at an incidence angle of 4 degrees is sent to the surface. Smallest acquisition angle was 10 degrees and the highest was 90 degrees. Each step was 0.02 degree, and scan speed was 0.6 deg/min. Figure 2.6. given shows the Bruker D8 Advanced XRD device.

Figure 2.6. Bruker D8 Advanced XRD device.

2.2.4. Atomic Force Microscopy

Atomic force microscopy (AFM) gives the surface topography information of the sample by moving an extremely sharp probe over its surface. Probe scans the surface by utilizing a scanner stage which is manufactured from a piezoelectric material. The probe consists of a cantilever beam with a molecularly sharp tip. Surface's roughness causes this probe

to be pushed or pulled as it travels the surface. The tip never touches the surface, it only approaches to it so that inter atomic forces start to act between the tip and the surface.

The bending of the probe due to these forces is measured with a laser light and morphology data is derived using computer programs [9]. A schematic representation of AFM device is provided in the Figure 2.7. below.

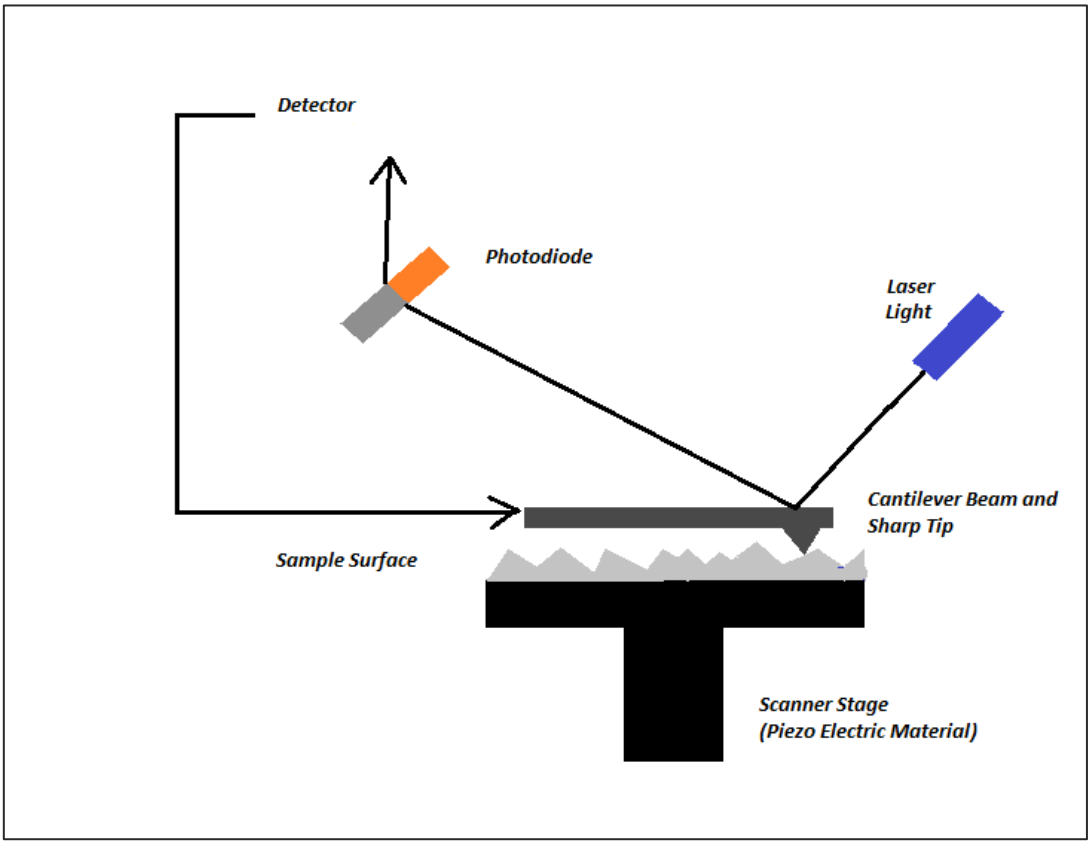

Figure 2.7. Representative setup of an AFM device [9].

The surfaces of uncoated and HEA coated NiTi samples were analyzed in this study using an AFM, Brucker, Dimension Icon device in tapping mode. The measurement area was 10 µm x 10 µm. The AFM device is shown in the Figure 2.8. below.

Figure 2.8. Brucker, Dimension Icon Atomic Force Microscope.

2.3. MECHANICAL PROPERTIES ANALYSIS

2.3.1. Nanoindentation

In nanoindentation, a certain amount of load is applied on the sample's surface with a sharp and extremely hard (mostly diamond) tip. Load is first applied, tip is kept in the loaded state for a certain amount of time to prevent any irregularities in indentation. Then unloaded causing the elastic deformation to be recovered. Upon this procedure, load and displacement data are recorded, hardness values and elastic moduli are calculated using elastic contact theory [9]. The term "nano" in this method indicates that both the applied load and created indentation are highly precise. Load can be in the range of 1 nN to 10 N

and indentation depth can be 1 nm to 20 μm [10]. The key point in the indentation test is to have an indenter having much higher hardness than the samples. In this study, an Agilent G200 depth-sensing nanoindentation machine was used in depth-sensing mode. Maximum load was 5 mN, loading and unloading rates were 0.5 mN/s. A Berkovich diamond tip was used as it is one of the best types of nanoindentation tips [10]. Tip is kept stable for 5 seconds. To prevent substrate effects, indentation depth was set to 1/10 of the thickness of the coating. 15 indentations were applied to each sample and average hardness and elastic moduli values were recorded with corresponding standard deviations. Agilent G200 nanoindentation machine is shown in the Figure 2.9. below.

Figure 2.9. Agilent G200 nanoindentation machine.

2.4. BIOACTIVITY AND BIOCOMPATIBILITY ANALYSIS

2.4.1. Immersion Tests

Immersion tests in this study were performed in order to investigate the bioactivities of the samples. Creating a similar environment with the body and immersing the samples inside this *in vitro* setup gives valuable information about bioactivity and biocompatibility of samples. In this study, simulated body fluid (SBF-blood) was prepared, uncoated and HEA coated 316 L stainless steel samples and bulk HEA samples were immersed inside. Samples were kept at 37 ºC for 1, 3, 5 and 7 weeks in separate polypropylene (PP) tubes. 20 ml SBF-blood was used for each 1 cm^2 surface area of sample. Chemical formula of a 1000 ml of SBF-blood is provided in the Table 2.1 below.

Table2.1. SBF-blood chemical formula [11].

Solution	Ingredients	Amount of Ingredients	pH
SBF-blood (1000 ml)	NaCl	8.036 g	7.4
	$NaHCO_3$	0.352 g	
	KCl	0.225 g	
	$K_2HPO_4.3H_2O$	0.230 g	
	$MgCl_2.6H_2O$	0.311 g	
	1 M HCl	40 ml	
	$CaCl_2.2H_2O$	0.293 g	
	Na_2SO_4	0.072 g	
	TRIS	6.063 g	
	1 M HCl	0.2 ml (for pH adjustment)	

At the end of each immersion period (1,3,5 and 7 weeks), samples were rinsed with distilled water and dried immediately. Immersion fluids were stored at 4 C^o inside PP tubes for ICP-MS analysis and samples were stored at room temperature inside sealed containers for SEM and EDS analyses. In the SEM and EDS examinations, hydroxyapatite particles were expected since they are bioactivity indicators. Immersion bath which was used is given in the Figure 2.10. below.

Figure 2.10. Water bath which was used for immersion tests.

2.4.2. Inductively Coupled Plasma Mass Spectrometry

ICPMS is a mass spectrometry device which can detect metallic and some non-metallic ions in test samples. Samples are taken into solution with dilute acids and ionized using inductively coupled plasma. It can identify and make quantitative analyses on even trace amounts of ionic constituents [12]. In this study, immersion fluids were diluted with ultra-pure distilled water for 20x dilution. Later, they were investigated using ICPMS to detect Cr and Ni ions that were possibly released from the sample. An Agilent 7700x ICP-MS device was used in the analyses and it is shown in the Figure 2.11. below.

Figure 2.11. Agilent 7700x ICP-MS device.

Bibliography

1. Jameson, E. *Electrical Discharge Machining. (Society of Manufacturing Engineers, 2001)*.

2. Kucukturk, G. & Cogun, C. A new method for machining of electrically nonconductive workpieces using electric discharge machining technique. *Mach. Sci. Technol.* **14,** 189–207 (2010).

3. Marashi, H., Sarhan, A. A. D., Maher, I. & Sayuti, M. *Techniques to Improve EDM Capabilities: A Review*. *Comprehensive Materials Finishing* **1–3,** (Elsevier Ltd., 2016).

4. Kingshott, P., Andersson, G., McArthur, S. L. & Griesser, H. J. Surface modification and chemical surface analysis of biomaterials. *Curr. Opin. Chem. Biol.* **15,** 667–676 (2011).

5. Silva-Molina, R. Boron Nitride and Carbon Nanostructures: Synthesis, Characterization and Ab Initio Calculations. (2015). doi:10.13140/RG.2.1.4269.5443

6. Bacon, S. Interactions between latent fingermarks , deposition surfaces and development agents Interactions between latent fingermarks , deposition surfaces and development agents . A thesis submitted for the degree of Master of Philosophy Simon Richard Bacon Brunel University. (2018). doi:10.13140/RG.2.2.15922.30400

7. Badami, A. S. Morphological and Structure-Property Analyses of Poly(arylene ether sulfone)-Based Random and Multiblock Copolymers for Fuel Cells. 159 (2007).

8. Bose, S. & Bandyopadhyay, A. in *Characterization of Biomaterials* 1–9 (2013). doi:http://dx.doi.org/10.1016/B978-0-12-415800-9.00001-2

9. Jaffe, M., Hammond, W., Tolias, P. and Arinzeh, T. *Characterization of Biomaterials.* (Woodhead Publishing Limited, Cambridge, 2013).

10. Ebenstein, D. M. & Pruitt, L. A. Nanoindentation of Nanoindentation has recently

emerged as a powerful tool for measuring. *Nano Today* **1,** 26–33 (2006).

11. Toker, S. M., Canadinc, D., Maier, H. J. & Birer, O. Evaluation of passive oxide layer formation-biocompatibility relationship in NiTi shape memory alloys: Geometry and body location dependency. *Mater. Sci. Eng. C* **36,** 118–129 (2014).

12. Godfrey, L. V. & Glass, J. B. The geochemical record of the ancient nitrogen cycle, nitrogen isotopes, and metal cofactors. *Methods Enzymol.* **486,** 483–506 (2010).

CHAPTER 3. MECHANICAL PROPERTIES OF TiTaHfNbZr HIGH-ENTROPY ALLOY COATINGS DEPOSITED ON NiTi SHAPE MEMORY ALLOY SUBSTRATES

TiTaHfNbZr high-entropy alloy (HEA) thin films with thicknesses of about 750 and 1500 nm were deposited on NiTi substrates by RF magnetron sputtering using TiTaHfNbZr equimolar targets. The thorough experimental analysis on microstructure and mechanical properties of deposited films revealed that the TiTaHfNbZr films exhibited amorphous and cauliflower-like structure, where grain size and surface roughness increased concomitant with film thickness. More importantly, the current findings demonstrate that the TiTaHfNbZr HEA films with mechanical properties of the same order as those of the NiTi substrate constitute promising biomedical coatings effective in preventing Ni release.

NiTi shape memory alloys (SMAs) are widely used in medical devices, such as orthopedic implants and prostheses, cardiovascular stents, and dental instruments, owing to their superior properties of superelasticity and shape memory effect [1–5]. Despite their superior mechanical properties, the biocompatibility of NiTi alloys has been a topic of debate [2,3]. Specifically, the long-term biocompatibility, bioactivity, and wear properties of NiTi SMAs give rise to concerns about the safety of their long-term utility in clinical applications [6,7]: out-diffusion of harmful Ni ions from the NiTi SMA during prolonged use inside human body poses several health risks [2,8,9]. In order to eliminate these risks, surface treatment of NiTi SMAs, namely the high-temperature oxidation, passivation, oxygen ion implantation, sol–gel, and PVD coating are commonly employed to introduce a layer of corrosion-resistant TiO2 on the surface, such that the allergic and toxic effects due to nickel release can be avoided [3,10–12]. However, the protection provided by the biocompatible yet brittle TiO2 layer is very short term in applications that are subjected to repeated and/or complex loads, [13,14] mainly due to the easy formation of cracks followed by Ni ion released from the freshly exposed NiTi SMA underneath the broken TiO2 layer [15].

In order to address this issue, attempts have been made to find suitable alternatives to conventional coating [16]. High-Entropy Alloys (HEAs), a new class of metallic materials with equimolar or near-equimolar compositions, constitute an example to this case, and they exhibit unprecedented excellent structural and functional properties that have recently attracted significant interest [15,17]. HEAs are usually composed of at least five principal elements, with concentrations between 5 and 35 atomic percent, [18] and because of the corresponding high mixing entropy, they usually form simple face-centered cubic (FCC) or body-centered cubic (BCC) solid-solution phase, and sometimes nanoscale or even amorphous structures [19]. Their simple structures and versatile physical and mechanical properties stem from their high mixing entropy, lattice distortion, sluggish diffusion, and cocktail effect [20]. Especially the HEAs composed of biocompatible constituents are potential candidates for utility as a new class of coatings on metallic biomaterials due to their superior mechanical properties, [21] which are also expected to overcome the coating–substrate property mismatch observed in the case of conventional coatings.

Among the various multicomponent HEAs, those consisting of nontoxic and allergy-free transition metals, such as Ti, Ta, Hf, Nb, and Zr, have been shown to fulfill these requirements: HEAs and their nitride and carbide films have been successfully deposited by physical vapor deposition (PVD) magnetron DC or RF sputtering methods [16,22–29]. In particular, the easy control of film structure and composition, good mechanical properties and uniform thickness of the coating, strong coating adhesion to the substrate, as well as the high rate of reproducibility, have made PVD magnetron sputtering a popular coating method [30,31]. However, despite the significant volume of studies focused on microstructure and mechanical properties of bulk HEAs considered for biomedical applications, with the exception of one work studying the mechanical properties and chemical response of carbides and nitrides of HEA coatings deposited on Ti6Al4V alloy in simulated body fluid, [16] neither a study of the structures and mechanical properties of PVD deposited biocompatible HEA films nor an assessment of their utility as metallic coating deposited on biomaterials has been forwarded yet [21]. This study was undertaken to address this issue, and the morphology and mechanical properties of the equimolar TiTaHfNbZr HEAs composed of biocompatible constituent elements deposited onto the NiTi SMA using the PVD method were studied.

In this study, an equimolar (20 at. percent for each element) $Ti_{20}Ta_{20}Hf_{20}Nb_{20}Zr_{20}$ target was prepared by arc melting of 99.99 percent pure constituent elements under vacuum and shaped into a disk of 50.8 mm in diameter and 6.3 mm in thickness. Samples with the size of 10 mm 910 mm 90.20 mm were cut from a commercial NiTi SMA (with 50.7 at. percent Ni) plate by electro discharge machining (EDM). In order to remove macrolevel surface defects and contaminants, the samples were ground using SiC emery papers, followed by final polishing to a mirror surface texture with a 0.30 μm alumina slurry. Polished samples were ultrasonically cleaned with acetone and rinsed with de-ionized water before the film deposition process. TiTaHfNbZr HEA films of two different thicknesses, namely 750 and 1500 nm, were deposited onto NiTi and silicon (100) substrates by RF magnetron sputtering (Nanovak NVTS-400). Deposited silicon samples were used for cross-sectional investigations and XRD analyses because of convenience in preparing samples by ion milling and improving signal-to-noise ratio. The films were deposited in an Ar atmosphere at room temperature and without substrate bias, where the chamber base pressure was below 1 9103 Pa and the Ar flow was kept at 10 standard cubic centimeters per minute (SCCM). For the sake of having a clean surface, the target was first pre-sputtered by Ar plasma for 10 minutes with a power of 80 W before deposition. After cleaning, the power was increased to 100 W and the shutter was opened.

The phase structures of the thin films were analyzed by grazing incidence X-ray diffraction (GIXRD-Bruker D8 Advanced) with Cu Ka radiation at an incidence angle of 4 deg and an acquisition angle ranging from 10 to 90 deg, with a 0.02 deg step and scan speed of 0.6 deg/ min. The cross-sectional micrograph and elemental depth profiles of HEA thin films were determined by SEM (Zeiss, Ultra Plus) equipped with energy dispersive X-ray spectrometer (EDS). The effects of deposition of films on surface morphology and roughness of NiTi substrate were examined by atomic force microscopy (AFM, Brucker, Dimension Icon). AFM measurements were acquired on a 10 μm x 10 μm area of the uncoated and coated samples in the tapping mode. The hardness values and elastic moduli of NiTi substrate and deposited films were measured by depth-sensing nanoindentation (Agilent G200) with Berkovich diamond indenter tip at a peak load of 5 mN, and the loading and unloading rates were set to 0.5 mN/s. In order to minimize material creep, a 5 second pause time was used between loading and unloading cycles. The penetration depth of the indenter was controlled at about 1/10 of the films' thickness,

and thus, a substrate effect could be neglected. At least, 15 measurements were performed on each sample, and the average values of hardness and elastic modulus with respective standard deviation were reported.

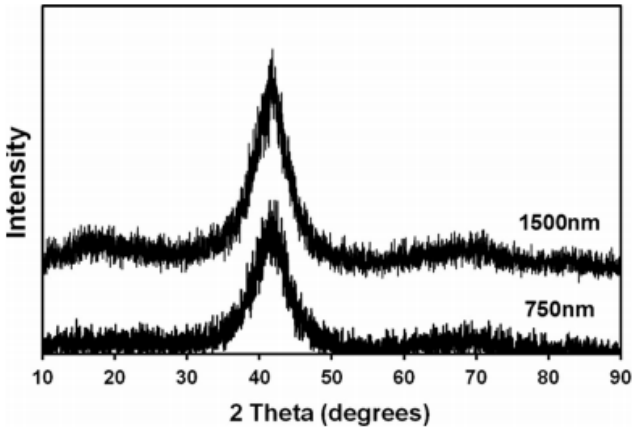

Figure 3.1. XRD patterns of the 750- and 1500-nm-thick TiTaHfNbZr HEA films.

XRD patterns of the 750- and 1500-nm-thick TiTaHfNbZr films are presented in Figure 3.1. For the deposited films shown in this figure, only a broad peak was observed, indicating an amorphous structure. This can be attributed to the low enthalpy, high mixing entropy, long-range diffusion and the large atomic size difference that favors the formation of amorphous structure [24,26,32–34]. From a thermodynamics point of view, low Gibbs free energy can increase the glass transition temperature, and consequently the glass forming ability: high configurational entropy and the low enthalpy due to low chemical potential have been shown to decrease Gibbs free energy at a constant temperature in multicomponent alloys [35]. In addition, diffusion of constituent elements and crystallization of films can be suppressed as a result of large difference between the deposition and glass transition temperatures of films, and the quenching-like effect of sputtering process [36].

Figure 3.2. shows the SEM morphologies of the surface and cross sections of TiTaHfNbZr HEA films deposited on NiTi and silicon substrates, respectively. A continuous ((b) and (d)) and cauliflower-like ((a) and (c)) morphology of TiTaHfNbZr films was evident for both 750- and 1500-nm-thick films. For the most part of the metallic film, the cauliflower-

like grains composed of numerous clusters with sizes ranging from several tens to hundreds of nanometers were observed [24,32]. A comparison of Figures 3.2(a) and (c) revealed that, as the coating thickness increases, coalescence of nanoparticles leads to development of slightly larger grains yet without a significant grain coarsening. This incremental increase in grain size of the 1500-nm-thick film can be attributed to the longer deposition time and the corresponding increase in deposited film temperature [37]. Although the structure of deposited films was analyzed as an amorphous phase, grain boundaries were observed (Figures 3.2(a) and (c)): the formation of a void network can result in density-deficient boundaries which are intrinsic to amorphous films [38,39]. Additionally, the wide black lines observed along the amorphous grain boundaries in Figures 3.2(a) and (c) are cracks caused by the internal stresses during deposition process [35,40,41]. It was reported that internal stresses increase concomitant with film thickness, leading to formation of deeper and wider cracks in deposited films [41]. It should be noted that, as opposed to the general idea that a thicker films would provide enhanced mechanical properties and prevention against harmful ion release form substrate, the formation of deep and wide cracks might lead to spallation and release of more allergenic and/or toxic elements in biomedical applications. Therefore, determining internal stress with varying thicknesses of deposited HEAs film plays a critical role in controlling ion release from NiTi substrate. However, controlling and reducing the internal stress of the films during deposition process is a complex phenomenon and is not within the scope of this research study.

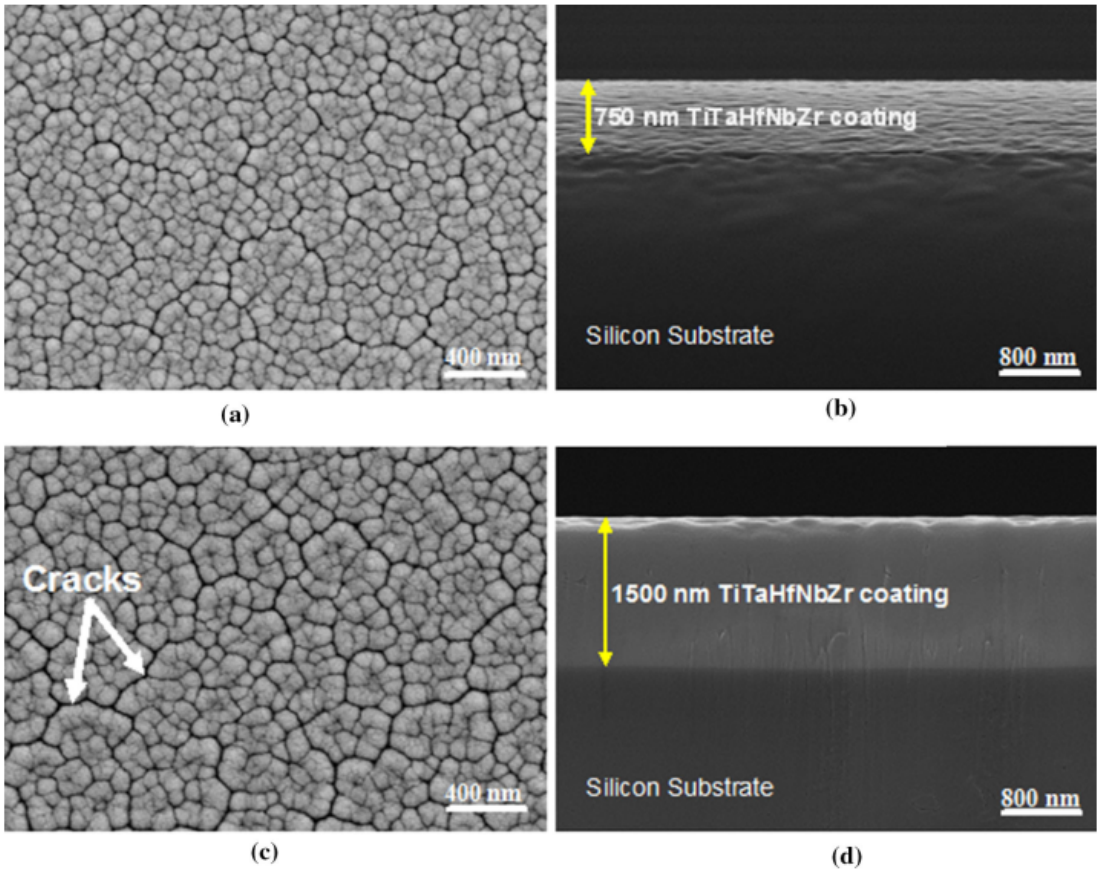

Figure 3.2. SEM images of the deposited HEA films: (a) and (c) plane view, and (b) and (d) cross-sectional images of 750- and 1500-nm thick TiTaHfNbZr HEA films.

The surface topography and roughness of the NiTi substrate and TiTaHfNbZr HEA films were determined by AFM (Figure 3.3.) Surface of NiTi substrate exhibited a smooth structure with a roughness of 2.84 nm, whereas following the deposition of the TiTaHfNbZr HEA coating and formation of cauliflower-like structures, the roughness values of 750- and 1500-nm-thick films were measured as 3.39 and 3.85 nm, respectively. Previous works reported that there is a correlation between the film thickness and surface roughness, such that continuing film growth increases the grain size, and thereby the surface roughness [24,32]. However, the relatively small differences in the measured roughness values of the current uncoated and TiTaHfNbZr-deposited NiTi SMAs can be attributed to amorphous structure of the HEA films [42]. In general, as crystalline films are deposited and continue to grow, the surface roughness increases since the film growth takes place faster on certain crystallographic planes [43]. However, in the case of

amorphous films, surfaces become smoother or planarized by continued deposition, which prevents a significant increase of roughness [43]. Despite the expected enhancement of biocompatibility, the observed lack of a significant increase in surface roughness by coating the NiTi surfaces with the TiTaHfNbZr HEA implies that the attachment of cells and other functional groups to the surface of the NiTi SMAs should not be expected to improve significantly [44,45]. However, based on recent evidence that the surface relief traces of fine microstructural features—such as slip and twinning, rather than the typical surface roughness dictate cell adhesion and proliferation on metallic surfaces, [44] this aspect should be investigated thoroughly with the aid of systematic cell culture and viability experiments, which is beyond the scope of the current study.

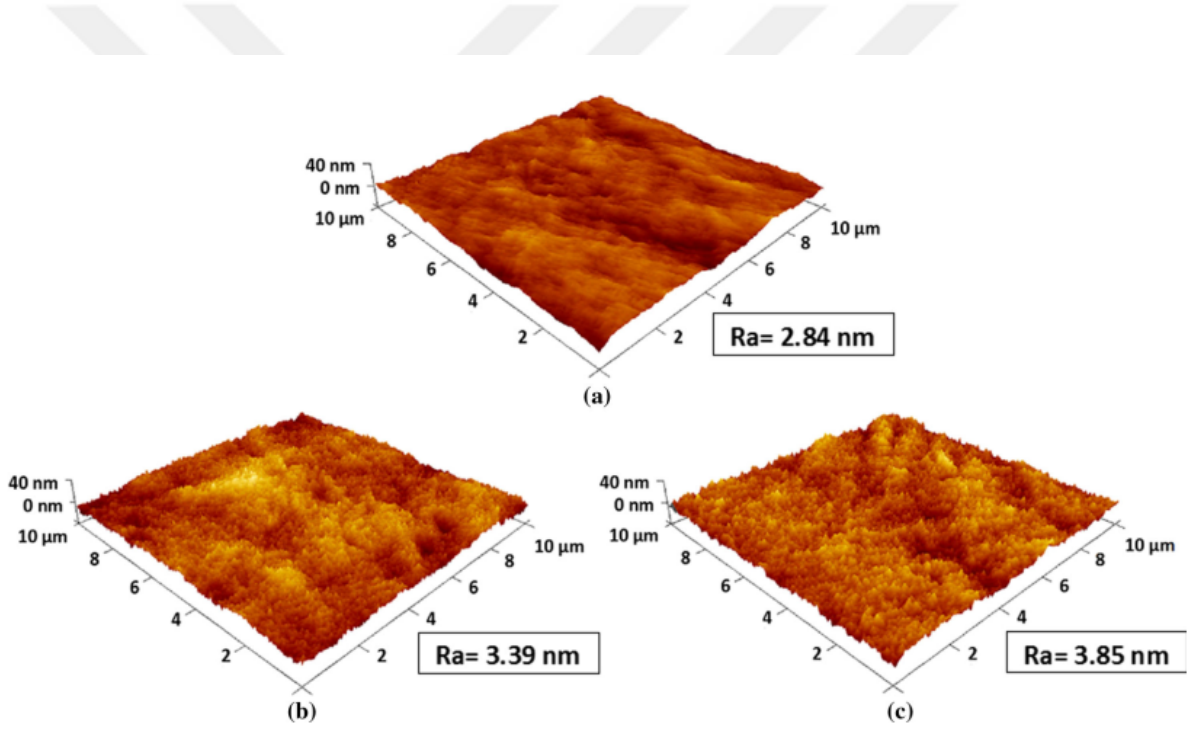

Figure 3.3. AFM images and surface roughness of (a) uncoated NiTi, and (b) 750- and (c) 1500-nm-thick TiTaHfNbZr HEA films.

The atomic concentrations of the constituent elements derived from the EDS quantitative analysis through the cross section of deposited films are plotted as concentration depth profile and presented in Figure 3.4. It can be clearly seen that the atomic percentage of each element in the films is rather close to that of the target and does not significantly

change with depth and film thickness, which is in good agreement with previous works [23,28,35]. Almost uniform elemental distribution within the deposited films is achieved owing to the fast quenching effect in the sputtering method [46]. Todai et al reported that the even distribution of the constituent elements has beneficial effect on biocompatibility of HEAs [21]. Furthermore, previous studies showed that chemical homogeneity result in even distribution of internal stress along the film thickness and reduce the risk of delamination or spallation of films under mechanical loads [46,47].

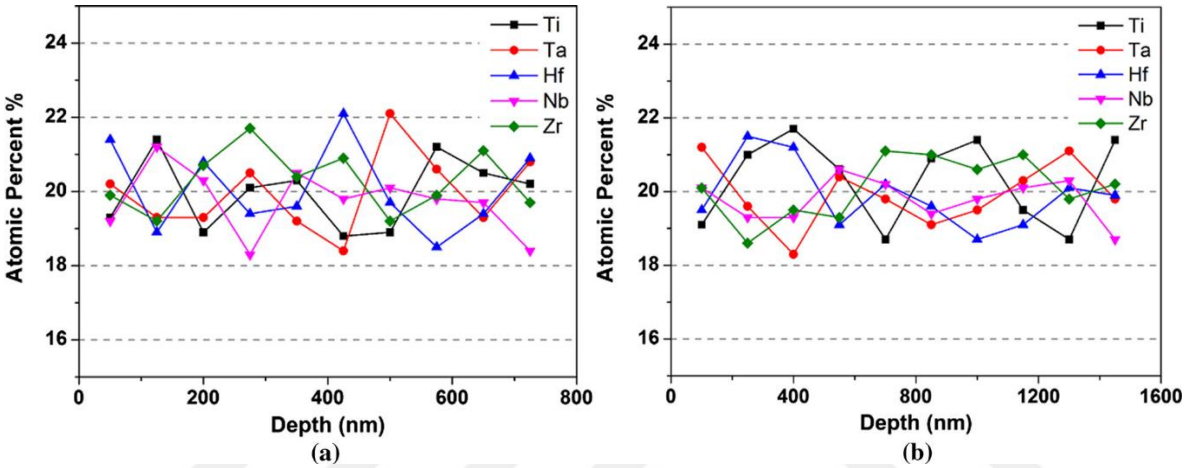

Figure 3.4. Concentration depth profiles of constituent elements in deposited (a) 750– and (b) 1500-nm-thick TiTaHfNbZr HEA films. Please note the scale difference between the x-axes.

From the loading–unloading curves and using Oliver and Pharr methods, hardness values and elastic moduli of NiTi substrate and TiTaHfNbZr HEA films were calculated (Table 3.1). The average values of the hardness and elastic modulus of the NiTi substrate are found to be 357 ± 25 HV and 67.2 ± 1.4 GPa, respectively. The films exhibited higher hardness and modulus values which are within the ranges of 1077 to 1330 HV and 169.7 to 185.8 GPa, respectively. Comparing with the as-cast or Hot isostatic-pressed alloy, TiTaHfNbZr films revealed remarkable enhancement in mechanical properties [48–52]. These superior mechanical properties stem from dense and smooth amorphous structure of the deposited films [35,53]. It is well known that the grain boundaries play a crucial role in impeding the dislocation motion and the resulting slip due to the differing grain

orientations and slip plane discontinuities from one grain to another. It should be noted that the slight reductions in both the modulus and hardness values of TiTaHfNbZr HEA film with the increasing film thickness can be associated with the coarsening of grains and formation of thicker cracks along grain boundaries [23,40]. The deposition of such an amorphous film with higher hardness can be beneficial in improving the wear resistance of coated NiTi SMAs employed in hip and knee joints. In addition, the lower and more stable friction coefficient of amorphous materials compared with crystalline materials [54,55] can be advantageous in these applications, considering the repeated abrasive loading conditions.

Table 3.1. Vickers Hardness Values and Elastic Moduli of the NiTi Substrate and the Deposited TiTaHfNbZr Coatings

	NiTi	*750 nm thick TiTaHfNbZr film*	*1500 nm thick TiTaHfNbZr film*
Hardness (HV)	357∓25	1285∓45	1132∓55
E (GPa)	67.2∓1.4	183.2∓2.3	172.8∓.1

Overall, the results presented herein demonstrate that the multicomponent TiTaHfNbZr HEA films with thickness of 750- and 1500 nm were deposited on NiTi substrates by RF magnetron sputtering exhibit a homogeneous layer ideal for preventing Ni release from the NiTi substrate. Furthermore, the mechanical properties of the HEA films are compatible with those of the NiTi substrate, which is crucial for preventing damage to the film due to mechanical loading in the long term, which in turn, enhances the protection against Ni release. Consequently, the current findings show that the equiatomic TiTaHfNbZr HEA can serve as an effective biocompatible coating to prevent Ni-ion release from NiTi implants.

Bibliography

1. S. Shabalovskaya, J. Anderegg, and J. Van Humbeeck: Acta Biomater., 2008, vol. 4, pp. 447–67.

2. H. Tian, D. Schryvers, D. Liu, Q. Jiang, and J. Van Humbeeck: Acta Biomater., 2011, vol. 7, pp. 892–99.

3. H. Wang, F. Liu, X. Xiong, S. Ke, X. Zeng, and P. Lin: Appl. Surf. Sci., 2015, vol. 356, pp. 1234–43.

4. Y.P. Zhang, D.S. Li, and X.P. Zhang: Scr. Mater., 2007, vol. 57, pp. 1020–23.

5. S.M. Toker and D. Canadinc: Mater. Sci. Eng. C. Mater. Biol. Appl., 2014, vol. 40, pp. 142–47.

6. C.L. Chu, T. Hu, S.L. Wu, Y.S. Dong, L.H. Yin, Y.P. Pu, P.H. Lin, C.Y. Chung, K.W.K. Yeung, and K. Chu: Acta Biomater., 2007, vol. 3, pp. 795–806.

7. F.T. Cheng, P. Shi, and H.C. Man: Scr. Mater., 2004, vol. 51, pp. 1041–45.

8. H.R. Wang, F. Liu, Y.P. Zhang, D.Z. Yu, and F.P. Wang: Appl. Surf. Sci., 2011, vol. 257, pp. 5576–80.

9. M.H. Elahinia, M. Hashemi, M. Tabesh, and S.B. Bhaduri: Prog. Mater. Sci., 2012, vol. 57, pp. 911–46.

10. R.M. Wang, C.L. Chu, T. Hu, Y.S. Dong, C. Guo, X.B. Sheng, P.H. Lin, C.Y. Chung, and P.K. Chu: Appl. Surf. Sci., 2007, vol. 253, pp. 8507–12.

11. L. Bait, L. Azzouz, N. Madaoui, and N. Saoula: Appl. Surf. Sci., 2017, vol. 395, pp. 72–77.

12. M.H. Wong, F.T. Cheng, and H.C. Man: Scr. Mater., 2007, vol. 61, pp. 3391–94.

13. D.P. Aun, M. Houmard, M. Mermoux, L. Latu-Romain, J.C. Joud, G. Berthome´ , and V.T.L. Buono: Appl. Surf. Sci., 2016, vol. 375, pp. 42–49.

14. S.M. Toker, D. Canadinc, H.J. Maier, and O. Birer: Mater. Sci. Eng. C., 2014, vol. 36, pp. 118–29.

15. L. Zhang, Y. Pengfei, H. Cheng, H. Zhang, H. Diao, Y. Shi, B. Chen, P. Chen, R. Feng, J. Bai, Q. Jing, M. Ma, P.K. Liaw, G. Li, and R. Liu: Mater. Sci., 2016, vol. 47, pp. 5871–75.

16. V. Braic, M. Balaceanu, M. Braic, A. Vladescu, S. Panseri, and A. Russo: J. Mech. Behav. Biomed. Mater., 2012, vol. 10, pp. 197–205.

17. Y. Liu, S. Ma, M.C. Gao, C. Zhang, T. Zhang, H. Yang, Z. Wang, and J. Qiao: Metall. Mater. Trans. A., 2016, vol. 47A, pp. 3312–21.

18. M.J. Yao, K.G. Pradeep, C.C. Tasan, and D. Raabe: Scr. Mater., 2014, vols. 72–73, pp. 5–8.

19. Y.F. Ye, Q. Wang, J. Lu, C.T. Liu, and Y. Yang: Scr. Mater., 2015, vol. 104, pp. 53–55.

20. D.B. Miracle and O.N. Senkov: Acta Mater., 2017, vol. 122, pp. 448–511.

21. M. Todai, T. Nagase, T. Hori, A. Matsugaki, A. Sekita, and T. Nakano: Scr. Mater., 2017, vol. 129, pp. 65–68.

22. D.-C. Tsai, Z.-C. Chang, L.-Y. Kuo, T.-J. Lin, T.-N. Lin, M.-H. Shiao, and F.-S. Shieu: Thin Solid Films., 2013, vol. 544, pp. 580–87.

23. M.-H. Hsieh, M.-H. Tsai, W.-J. Shen, and J.-W. Yeh: Surf. Coat. Technol., 2013, vol. 221, pp. 118–23.

24. B. Ren, Z. Shen, and Z. Liu: J. Alloys Compd., 2013, vol. 560, pp. 171–76.

25. V. Dolique, A. Thomann, P. Brault, Y. Tessier, and P. Gillon: Surf. Coat. Technol., 2010, vol. 204, pp. 1989–92.

26. C.H. Lin, J.G. Duh, and J.W. Yeh: Surf. Coat. Technol., 2007, vol. 201, pp. 6304–08.

27. C.-H. Lai, M.-H. Tsai, S.-J. Lin, and J.-W. Yeh: Surf. Coat. Technol., 2007, vol. 201, pp. 6993–98.

28. C.-H. Lai, S.-J. Lin, J.-W. Yeh, and S.-Y. Chang: Surf. Coat. Technol., 2006, vol. 201, pp. 3275–80.

29. P.-K. Huang and J.-W. Yeh: Scr. Mater., 2010, vol. 62, pp. 105–08.

30. D.B. Miracle, J.D. Miller, O.N. Senkov, C. Woodward, M.D. Uchic, and J. Tiley: Entropy., 2014, vol. 16, pp. 494–525.

31. R. Rodr, J.A. Benito, E.S. Puchi-cabrera, and M.H. Staia: Wear., 2007, vol. 262, pp. 380–89.

32. B. Ren, Z.X. Liu, L. Shi, B. Cai, and M.X. Wang: Appl. Surf. Sci., 2011, vol. 257, pp. 7172–78.

33. S. Guo: Mater. Sci. Technol., 2015, vol. 31, pp. 1223–30.

34. A. Inoue: Mater. Trans. JIM., 1995, vol. 36, pp. 866–75.

35. L. Liu, J.B. Zhu, C. Hou, J.C. Li, and Q. Jiang: Mater. Des., 2013, vol. 46, pp. 675–79.

36. T.-K. Chen, M.-S. Wong, T.-T. Shun, and J.-W. Yeh: Surf. Coat. Technol., 2005, vol. 200, pp. 1361–65.

37. X. Li, Z. Zheng, D. Dou, and J. LiEngineering Training Centre: Mater. Res., 2016, vol. 19, pp. 802–06.

38. T.M. Donovan and K. Heinemann: Phys. Rev. Lett., 1971, vol. 27, pp. 1794–96.

39. S. Tsukimoto, M. Moriyama, and M. Murakami: Thin Solid Films., 2004, vol. 460, pp. 222–26.

40. C.-H. Tsau, Z.-Y. Hwang, and S.-K. Chen: Adv. Mater. Sci. Eng., 2015, vol. 2015, pp. 1–7.

41. M. Ta ˆ rcolea, V. Soare, M. Burada, I. Constantin, D. Mitric, V. Ba ˘ dilita ˘ , and A. Caragea: Appl. Surf. Sci., 2015, vol. 358, pp. 533-39.

42. C.H. Lin, J.G. Duh, and J.W. Yeh: Surf. Coat. Technol., 2007, vol. 201, pp. 6304–08.

43. M. Donald: Mattox: Handbook of Physical Vapor Deposition (PVD) Processing, 2nd ed., Elsevier Inc, Oxford, 2010.

44. B. Uzer, S.M. Toker, A. Cingoz, T. Bagci-onder, G. Gerstein, and H.J. Maier: J. Mech. Behav. Biomed. Mater., 2016, vol. 60, pp. 177–86.

45. T. Sun, L.P. Wang, M. Wang, H.W. Tong, and W.W. Lu: Thin Solid Films., 2011, vol. 519, pp. 4623–28.

46. Z. An, H. Jia, Y. Wu, P.D. Rack, A.D. Patchen, Y. Liu, Y. Ren, N. Li, and P.K. Liaw: Mater. Res. Lett., 2015, vol. 3, pp. 203–09.

47. D.-C. Tsai, Z.-C. Chang, B.-H. Kuo, T.-N. Lin, M.-H. Shiao, and F.-S. Shieu: Surf. Coat. Technol., 2014, vol. 240, pp. 160–66.

48. J. Vesely ´ , J. Zy ´ ka, J. Ma ´ lek, Z. Pala, and I. Andrsˇ ova ´ : In _ Met. 2015, Brno, Czech Republic, 2015, pp. 3–8.

49. M.-H. Tsai, J.-W. Yeh: Mater. Res. Lett., 2016, vol. 3831.

50. B.S. Murty, J.W. Yeh, and S. Ranganathan: High-Entropy Alloys, Elsevier, Amsterdam, 2014.

51. O.N. Senkov, J.M. Scott, S.V. Senkova, D.B. Miracle, and C.F. Woodward: J. Alloys Compd., 2011, vol. 509, pp. 6043–48.

52. N. Larianovsky, A. Katz-Demyanetz, E. Eshed, and M. Regev: Materials (Basel)., 2017, vol. 10, pp. 1–12.

53. S.-Y. Chang, S.-Y. Lin, Y.-C. Huang, and C.-L. Wu: Surf. Coat. Technol., 2010, vol. 204, pp. 3307–14.

54. H.R. Ma, X.Y. Chen, J.W. Li, C.T. Chang, G. Wang, H. Li, X.M. Wang, and R.W. Li: Surf. Eng., 2017, vol. 33, pp. 56–62.

55. A. Moreira, R. Junio, C. Batista, L. Anderson, M. Martins, M. Ilha, M. Queiroz, D. Rodrigues, F. Costa, R. Guma, I. Lourdes, and T. Matte: Corros. Sci., 2014, vol. 82, pp. 297–303.

CHAPTER 4. TiTaHfNbZr HIGH ENTROPY ALLOY AS A BIOMEDICAL COATING ON METALLIC IMPLANT MATERIALS

1000 nm thick TiTaHfNbZr and $Ti_{1.5}Ta_{0.5}Hf_{0.5}Nb_{0.5}Zr$ high entropy alloy coatings were deposited on 316L stainless steel (SS) substrates by RF magnetron sputtering (PVD). Microstructural, mechanical, bioactivity and biocompatibility tests were held to investigate the performance of HEA coating as a novel surface modification method. Results concluded that PVD coating of HEAs forms uniform and amorphous HEA films having cauliflower-like structures. HEA coatings slightly decrease the Young's Modulus of uncoated 316L SS whereas they triple the hardness. Bioactivities of the substrates were improved with this surface modification technique. However, Ni ion release behavior depends on the coating quality. Uniformly coated films prevent the release better than spontaneously formed oxide layer on the uncoated 316L SS. On the other hand, faulty coating results in more ion release probably due to pitting corrosion.

1. Introduction

Metallic biomaterials are accounted as the most vital and widely used group of biomaterials thanks to their specific assets. They have advanced mechanical properties such as strength, hardness and elastic modulus. They are formable and their properties can be tailored with alloying. However, their wear and corrosion resistances are rather weak, and their biocompatibility is open to questions. For these reasons surface treatment is essential. 316 L stainless steels are one of the most widely used metallic implant materials, especially in fracture fixation and stent applications. Having Cr and Ni as main alloying elements, they have passive oxide layer on their surfaces (Cr_2O_3) and they have austenitic FCC structure. These make them corrosion resistant and nonmagnetic [1]. Both assets are crucial for a durable implant material. This low-cost material is accepted to be biocompatible but studies showed that in long-term usage, Ni ion release causes nickel poisoning which leads to inflammation, skin rash, narrowing of blood vessels and fibrinogenesis around the implant [2]. In fact, an oxide layer composed mainly of Cr_2O_3 spontaneously forms on the 316L SS's surface. It can also be artificially formed with

thermal oxidation. In commercial implants, this oxide layer is used as a shield for metal ion release. For a short duration, this prevents Ni ion release and supplies a suitable contact surface for the surrounding tissue. However, being a thin ceramic layer, this oxide film is highly prone to cracking and flaking off. This deteriorates the ion release protection since the uncoated 316L SS is now in contact with the surrounding tissue. Specifications of a coating material should be decided in accordance with the application. Metallic implants are generally used in orthodontics and orthopedics as load-bearers. So, it is indispensable to have excellent mechanical properties in the coating material too. In addition, since the material will be surrounded with living tissue and bone cells (osteoblasts, osteocytes ad osteoclasts), coating material cannot be toxic and should supply maximum protection against toxic leakage from substrate. However, being strong and non-toxic is not enough. A coating material for an orthopedics implant must also be osteoconductive, it must be convenient for bone cells and minerals to reside on [3]. Considering these requirements, it is inevitable that a brittle oxide layer does not provide a suitable coating. This study offers a more durable and biocompatible coating material, a high entropy alloy, which can withstand load-bearing applications together with corrosive and/or abrasive environments. High entropy alloys (HEAs) consist of minimum five metals combined in a nearly or completely equiatomic compositions. They are in FCC or BCC solid solution structure of their elements thanks to high mixing entropy. Their highly distorted lattice structure acts as a barrier to both dislocation propagation and diffusion thus strengthens the structure [4,5]. Along with high mixing entropy and distorted lattice structure, they have cocktail effect. This means that their final properties are associated to not only the individual elements forming the alloy but also to the reactions between subgroups of constitutive elements [6]. The specific HEA used in this study as a coating material for 316L SS substrates is TiTaHfNbZr. In the earlier studies, mechanical properties, microstructure and tribology of TiTaHfNbZr coatings on various commercial biomaterials have been studied [4,7]. However, their bioactivity and biocompatibility behavior remained away from the interest. In the current work, 316L SS substrates were PVD coated with TiTaHfNbZr and $Ti_{1.5}Ta_{0.5}Hf_{0.5}Nb_{0.5}Zr$ using RF Magnetron Sputtering and some of them were finally thermally oxidized. Mechanical, microstructural and *in vitro* biocompatibility and bioactivity tests were conducted on coated 316L stainless steels. Results showed that TiTaHfNbZr HEA is a promising coating

material since it has excellent mechanical properties, inhibits toxic ion release and communicates well with the surrounding tissue. These results are in accordance with the nature of the selected HEA because composing elements are non-toxic and sluggish diffusion effect can perform an effective barrier for ion release from substrate.

2. Experimental Procedure

The high entropy alloy targets (equimolar TiTaHfNbZr and $Ti_{1.5}Ta_{0.5}Hf_{0.5}Nb_{0.5}Zr$) were prepared in a vacuum arc melting device by mixing 99.99% pure elements. Both targets were 6.3 mm thick discs with 50.8 mm diameters. In addition to target discs that will be used for PVD coating, the two HEA rods were also cast. HEA substrates with 10 mm x 5mm x 1 mm dimensions were cut from these rods with electrical discharge machining (EDM). 316 L stainless steel substrates were also cut with EDM into 1 mm thick discs having 10 mm diameters. To prepare smooth and clean surfaces which are necessary for PVD coating, substrate surfaces were grinded with 120 to 2000 grit SiC emery papers and polished with 0.30 μm alumina slurry. Finally, samples were cleaned using ultrasonic cleaner respectively with ethanol, acetone and distilled water and air-dried. 1000 nm HEA coating of disc shaped 316 L samples were carried on a Nanovak NVTS-400 PVD device by RF magnetron sputtering. For each target, a separate silicon (100) wafer was also coated and cross-sectional SEM images were taken to investigate the coating uniformity and continuity. These wafers were also used to set the most suitable signal-to-noise ratio for XRD analyses. Silicon wafers were chosen merely because they ease the sample preparation procedure. The deposition took place under Ar gas flowing with a rate of 10 standard cubic centimeters per minute (SCCM) at room temperature. There was no substrate bias, sputtering power was 100 W and base pressure of the chamber was less than 1 x 10^{-5} Pa during whole process. Since the targets were open to atmosphere, impurities form on their surface. In order to deposit a uniform and pure coating, targets were pre-sputtered with a power of 80 W for 10 minutes by Ar plasma. For each target, 8 different 316L substrates, in total 16 substrates were coated. 4 of these 8 substrates were thermally oxidized at 300 C° air atmosphere for 5 minutes. To check whether the desired atomic percentages were reached during target and bulk HEA production, XRF analyses were conducted in a Bruker Tiger S8 X-ray Fluorescence Spectrometer device.

Commercially bought 316 L stainless steel substrates were also checked in the same regard. XRD analyses were conducted on a Bruker D8 Advanced X-Ray Diffractometer with Cu Kα radiation to investigate the phases present in bulk HEAs, 316 L stainless steel uncoated substrates and HEA coatings. Since the coating thickness is 1000 nm, a grazing incidence angle of 4 degrees was adequate. Acquisition range was in between 10 to 90 degrees, each step was 0.02 degrees and scan speed was 0.6 deg/min. Mechanical properties such as Young's modulus and hardness of uncoated 316 L stainless steel, two bulk target HEAs and HEA coated stainless steel substrates were also measured as previously explained in Chapter 3. Continuity and uniformity of HEA coatings were observed with Zeiss Ultra Plus Scanning Electron Microscope (SEM) prior to bioactivity and biocompatibility tests. SEM images of top and cross-sectional view of coatings on silicon wafer were taken. To take cross-sectional images, coated substrates should be cut. To spare actual substrates, silicon wafer was used since it represents 316 L stainless steel substrates. Bioactivity and biocompatibility analyses were performed after the samples were immersed in artificial blood (c-SBF). SBF was prepared in a polypropylene (PP) beaker according to the Table 4.1 below and its pH is around 7.4.

Table 4.1. Chemical ingredients of artificial blood.

Ingredients	Amount of Ingredients (g/l)
NaCl	8.036
$NaHCO_3$	0.352
KCl	0.225
$K_2HPO_4.3H_2O$	0.230
$MgCl_2.6H_2O$	0.311
1 M HCl	40 ml
$CaCl_2.2H_2O$	0.293
Na_2SO_4	0.072
TRIS	6.063
1 M HCl	0.2 ml (add until the pH is 7.4)

Each sample immersed in a separate PP centrifuge tube regarding to the following ratio:

$$\frac{surface\ area}{SBF\ volume} = \frac{1}{20}\ cm^2/ml$$

32 centrifuge tubes were stored in 37 °C water bath for 1, 3, 5 and 7 weeks. Each week has the same group of seven samples: uncoated 316 L stainless steel, bulk TiTaHfNbZr, bulk $Ti_{1.5}Ta_{0.5}Hf_{0.5}Nb_{0.5}Zr$, TiTaHfNbZr coated 316 L SS, TiTaHfNbZr coated and oxidized 316 L SS, $Ti_{1.5}Ta_{0.5}Hf_{0.5}Nb_{0.5}Zr$ coated 316 L SS and $Ti_{1.5}Ta_{0.5}Hf_{0.5}Nb_{0.5}Zr$ coated and oxidized 316 L SS samples. At the end of each immersion period, samples were rinsed with distilled water, air dried and stored for SEM analyses on Zeiss Evo LS15 and Zeiss Ultra Plus Scanning Electron Microscopes. In these analyses, hydroxyapatite (HA) formation on their surfaces was investigated to understand the bioactivity performances of the coatings. Earlier studies showed that HA is the inorganic mineral phase of bone tissues [8]. So, HA layer formation observed via SEM gives information about the bioactivity of coatings. To distinguish HA particles from any other surface impurity, energy dispersive X-ray spectrometer (EDS) was used together with SEM. For biocompatibility tests, immersion fluid was subjected to ICP-MS analysis in an Agilent7700x ICP-MS device. Ni and Cr ion releases from 316 L stainless steels to the immersion fluids were measured. Since the readings from 10 X diluted and non-diluted immersion fluids were similar, all fluids were 10 X diluted. For dilution, 2 % SUPRAPURE grade % 65 HNO_3 was added to ultra-pure water and this mixture was used. Nitric acid returns any compounds of Ni or Cr to the ion form. Maximum calibration point for the analysis was 50 ppb and minimum point was 0.78 ppb. The device took 5 measurements from each week's immersion fluid.

3. Results and Discussion

The results of XRF analysis are given in the Tables 4.2 and 4.3 below. They prove that the arc melting performed to cast target and substrate HEA materials was well-directed and the aimed atomic percentages were reached. Weight percentages of commercially bought 316 L SS also meets the ASTM F138 and F139 requirements in a great extent, each element is in the correct amount except the Ni content is slightly less than the standards.

Table 4. 2. Weight percentages of commercial 316 L stainless steel substrates.

Sample (wt%)	Cr	Cu	Mn	Mo	Ni	Ca	Si	Fe	V	Co
316L SS	17	0.388	1.54	2.03	9.76	0.057	0.33	68.11	0.079	0.16

Table 4.3. Atomic percentages of TiTaHfNbZr and $Ti_{1.5}Ta_{0.5}Hf_{0.5}Nb_{0.5}Zr$.

Sample (at%)	Ti	Ta	Hf	Nb	Zr
TiTaHfNbZr	19.75	20.38	20.93	19.18	19.76
$Ti_{1.5}Ta_{0.5}Hf_{0.5}Nb_{0.5}Zr$	35.86	12.50	12.84	11.79	27.02

As explained in the Chapter 1, these accurate atomic percentages of HEAs lead the four main phenomena of high entropy alloys to take place: high entropy, lattice distortion, cocktail and sluggish diffusion effects. Since all five elements exist in remarkable amounts, they contribute to high entropy of mixing and this stabilizes solid solution phase. Different atomic radii of various randomly distributed elements distort the lattice in a great manner. By definition, cocktail effect arises from the interactions between the constituting elements and the more elements exist in the lattice, the more this effect is pronounced. In a HEA lattice structure, there are many different atomic sites. Some of these sites have low lattice potential energy (LPE) and they cause diffusion rates to drop, creating sluggish diffusion effect. As expected, sluggish diffusion hinders phase transformation too [9,10]. The XRD patterns of 316 L stainless steel, bulk TiTaHfNbZr, bulk $Ti_{1.5}Ta_{0.5}Hf_{0.5}Nb_{0.5}Zr$, TiTaHfNbZr coating on silicon wafer, $Ti_{1.5}Ta_{0.5}Hf_{0.5}Nb_{0.5}Zr$ coating on silicon wafer were given respectively in the Figure 4.1. (a) to (e) below:

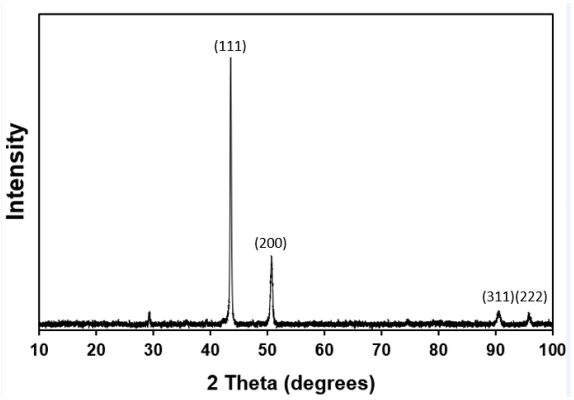

(a)

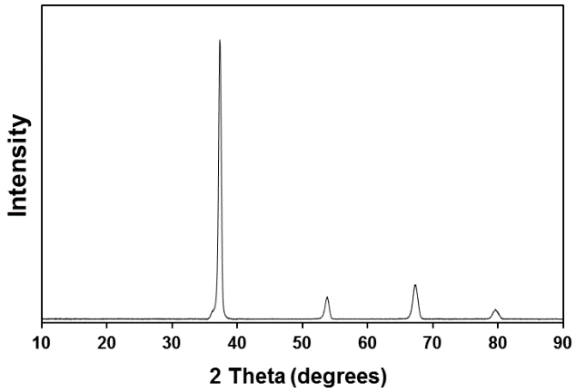

(b)

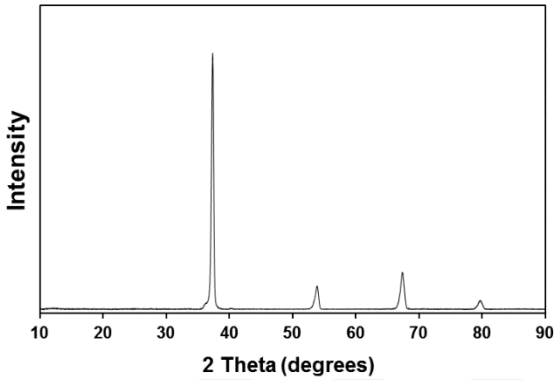

(c)

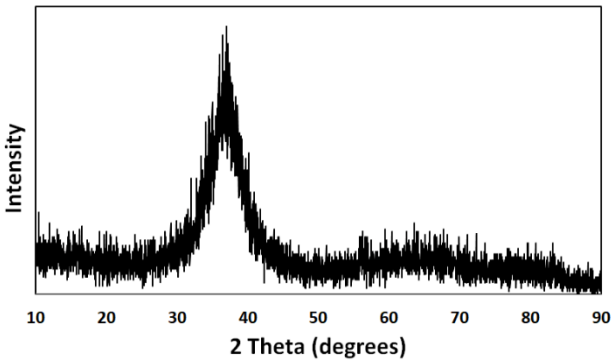

(d)

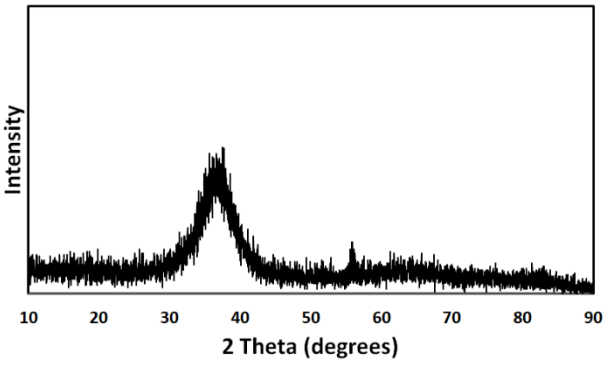

(e)

Figure 4.1. XRD patterns of (a) 316 L stainless steel, (b) bulk TiTaHfNbZr, (c) bulk $Ti_{1.5}Ta_{0.5}Hf_{0.5}Nb_{0.5}Zr$, (d) TiTaHfNbZr coating on silicon wafer and (e) $Ti_{1.5}Ta_{0.5}Hf_{0.5}Nb_{0.5}Zr$ coating on silicon wafer.

Austenitic 316L stainless steel shows a typical crystalline structure pattern since it has FCC structure [11]. However, as most of the HEAs, TiTaHfNbZr and $Ti_{1.5}Ta_{0.5}Hf_{0.5}Nb_{0.5}Zr$ bulks are rather new materials and their lattice parameters are not found in the XRD programs' libraries. For this reason, their peaks could not be labeled. Yet, it is known that they are rather FCC or BCC solid solutions. Coatings of these two high entropy alloys however, showed typical XRD patterns of amorphous structures. Although HEAs are known with having crystalline structures, it was also pronounced that they may have amorphous structures when certain conditions apply [4,12]. An alloy's preference between amorphous and crystalline structures depends on glass formation ability of that alloy [13]. According to Jien-Wei Yeh, rapid solidification and thin film coatings of HEAs tend to form amorphous structures. Along with these, an important approach called "confusion principle" was introduced by Turnbull and Greer. The principle states that increasing the number of constituting elements prevents a definite crystal structure to exist in the lattice and enhances glass formation ability. Together with high entropy and sluggish diffusion effects, confusion principle arising from varying atomic radii of the elements impels the structure to be amorphous [14]. Topological dense packing of the structure resulting from confusion principle increases viscosity and thus glass forming ability [15]. Inoue states that the minimum atomic size difference which is enough to cause confusion principle is 12 % [16]. Atomic size difference is generally defined by δ.

$$\delta = \sqrt{\sum_{i=1}^{n} c_i \left(1 - \frac{r_i}{\bar{r}}\right)^2}$$
$$\bar{r} = \sum_{i=1}^{n} c_i r_i$$

c_i is atomic percentage and r_i is atomic radius of the i^{th} component. In the current study of TiTaHfNbZr and $Ti_{1.5}Ta_{0.5}Hf_{0.5}Nb_{0.5}Zr$, when empirical atomic radii are taken into consideration, none of the element couples lead to confusion principle [17]. When calculated values of atomic radii are compared, there are significant size differences between Ti-Ta, Ti-Hf and Ti-Zr since Ti has the smallest atomic radius among these five elements [18]. With these being mentioned, it is worth to say that confusion principle might have taken an active role on amorphous phase formation. In kinetic point of view, RF magnetron sputtering suppressed long-range diffusion due to rapid solidification. Yeh states that even 1 hour of deposition process in a deposition temperature of 400-500 °C is enough to prevent crystallization. Considering that the HEA coatings in this study were

deposited at room temperature, a quenching-like process took place. What pronounces this quenching-like mechanism even more is sluggish diffusion effect. Unlike traditional alloys, multi-components of HEA collaborates with rapid cooling and inhibits crystallization [14]. Other than atomic size difference, multi-components, rapid solidification and sluggish diffusion, thermodynamic concepts play an important role on HEAs' glass forming ability in a great extent. Below formula of Gibbs free energy is the main starting point for almost all interpretations about thermodynamics behind amorphous phase formation.

$$\Delta G_{mix} = \Delta H_{mix} - T\Delta S_{mix}$$

Entropy of mixing, ΔS_{mix}, increases with increasing number of components. Also, studies showed that highest entropy is reached when all elements are in equal atomic ratios [12,15]. The alloy's preference to form an amorphous phase depends on ΔH_{mix} and ΔS_{mix} comparison. So, a new parameter Ω, is defined.

$$\Omega = \frac{T_m \Delta S_{mix}}{|\Delta H_{mix}|}$$

Elements that favor glass formation mostly have negatively large enthalpies. Solid solutions are stable when ΔH_{mix} is near zero and when large values of $T_m\Delta S_{mix}$ are obtained since high entropy increases solubility of elements between each other. Previous studies proved that high values of δ together with small Ω values lead to amorphous phase [12,15,19].

Elastic moduli, and hardness values of the bulk materials and coatings are given in the Table 4.4 below.

Table 4.4. Mechanical properties of bulk 316 L SS, TiTaHfNbZr, $Ti_{1.5}Ta_{0.5}Hf_{0.5}Nb_{0.5}Zr$ and HEA coated 316 L SS samples.

	316L SS	**TiTaHfNbZr**	**$Ti_{1.5}Ta_{0.5}Hf_{0.5}Nb_{0.5}Zr$**	**TiTaHfNbZr coated 316 L SS**	**$Ti_{1.5}Ta_{0.5}Hf_{0.5}Nb_{0.5}Zr$ coated 316 L SS**
E (GPa)	216.8	113.9	97.4	187.5	170.2
Hardness (HV)	362	371.2	333.4	1142	1030

These values were calculated by applying Oliver and Pharr methods to data collected from nanoindentation tests. There is a moderate decrease in elastic modulus of 316 L SS substrate after HEA deposition but an outstanding increase in hardness. This is attributed to the amorphous HEA coating which supplies a wear resistant layer [4]. However, since the mechanical behavior of these coatings are out of the scope of this chapter, more detailed information was given in the Chapter 3 about TiTaHfNbZr coating on NiTi substrate. Cross sectional and top view SEM images of HEA coatings on silicon wafer were taken to investigate coating quality. Images are given in the Figure 4.2. (a) to (d) below.

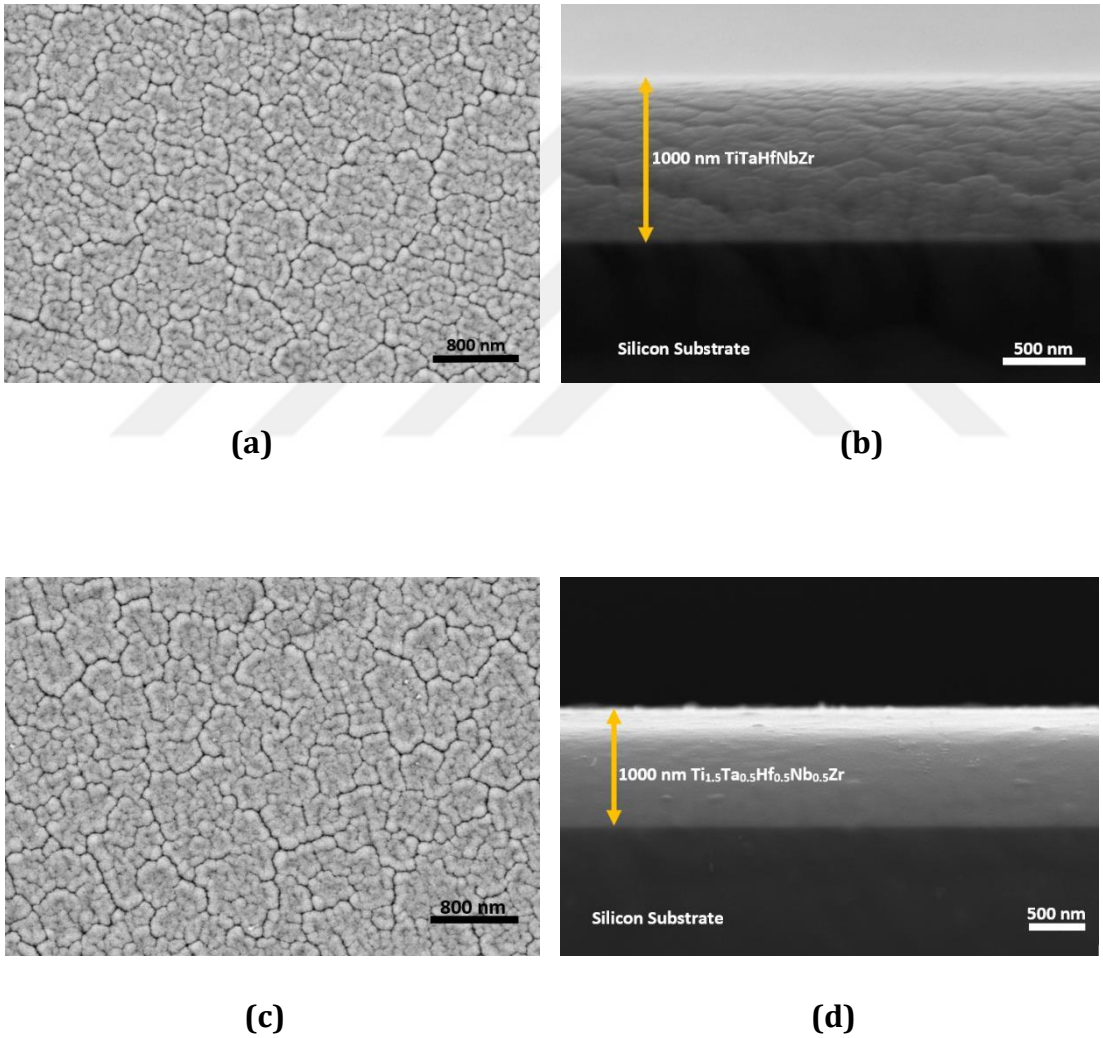

Figure 4.2. SEM images of (a) top view and (b) cross-sectional view of 1µ TiTaHfNbZr coating on silicon wafer. (c) Top view and (d) cross-sectional view images of 1µ $Ti_{1.5}Ta_{0.5}Hf_{0.5}Nb_{0.5}Zr$ coating on silicon wafer.

Both Figure 4.2. (a) and (c) show the cauliflower-like grains of the amorphous HEA coating, there is no appreciable difference. Grains are composed of small round-shape segments and grain boundaries appear darker. Grain boundaries are in fact cracks and they are usually formed due to internal stress and atomic size differences between constituent elements [20]. Cracks constitutes the risk of mechanical deformation of the film and ion release from the substrate. Inhibiting these cracks is possible with shortening the deposition time and decreasing the film thickness. This will decrease the grain sizes, thus causes a harder and more corrosion resistant HEA layer [4,7,21]. Grain sizes vary but diameters of small segments are mostly between 50 nm to 150 nm for both coatings. Figures (b) and (d) prove that the coating thickness is uniform, and the coating is continuous. After the immersion tests, surfaces of the samples were investigated with SEM and EDS.

SEM images of first week's samples are given in the Figure 4.3. below.

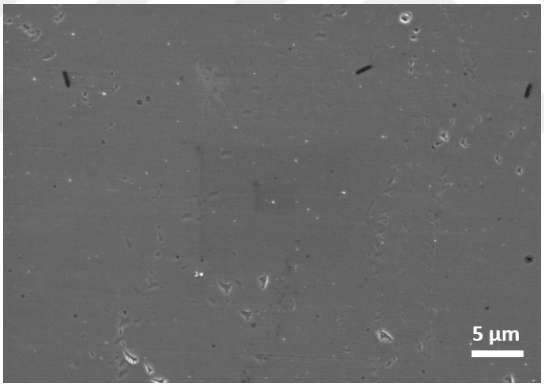

(a)

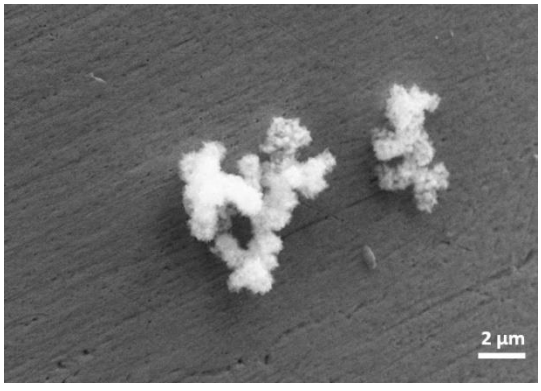

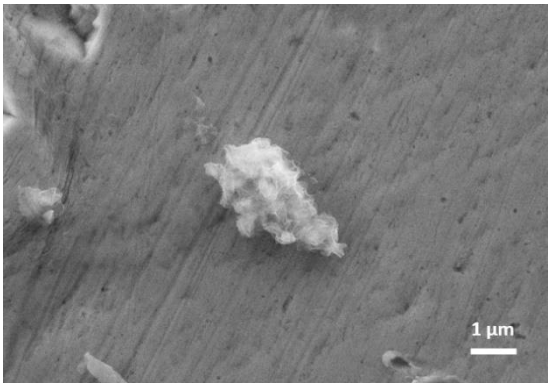

(b) **(c)**

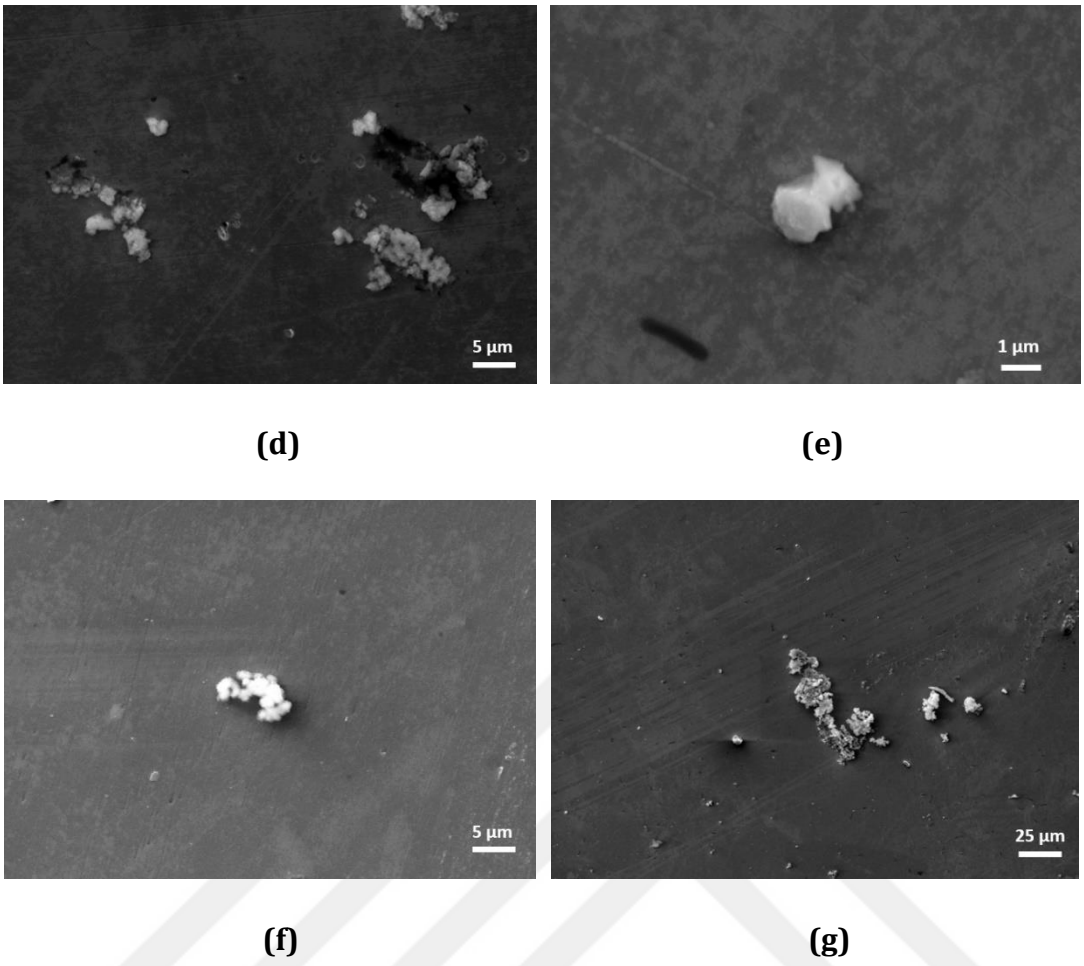

Figure 4.3. After 1 week of immersion, SEM images taken from (a) 316 L stainless steel, (b) bulk TiTaHfNbZr, (c) bulk $Ti_{1.5}Ta_{0.5}Hf_{0.5}Nb_{0.5}Zr$, (d) TiTaHfNbZr coating on 316L SS, (e) oxidized TiTaHfNbZr coating on 316 L SS, (f) $Ti_{1.5}Ta_{0.5}Hf_{0.5}Nb_{0.5}Zr$ coating on 316L SS and (g) oxidized $Ti_{1.5}Ta_{0.5}Hf_{0.5}Nb_{0.5}Zr$ coating on 316L SS.

Figure 4.3. shows the hydroxyapatite (HA) particles nucleated on the surfaces of samples. 1 week is a short duration for making interpretations but it is evidential that HEA bulks and HEA coatings showed better apatite forming performance than 316L stainless steel, which does not have any nucleation. Particles formed on bulk TiTaHfNbZr, bulk $Ti_{1.5}Ta_{0.5}Hf_{0.5}Nb_{0.5}Zr$, TiTaHfNbZr coating on 316L SS ,oxidized TiTaHfNbZr coating on 316 L SS and $Ti_{1.5}Ta_{0.5}Hf_{0.5}Nb_{0.5}Zr$ coating on 316L SS are separated from each other and their diameters around 5µm as in the previous works found in the literature [22,23]. However, oxidized $Ti_{1.5}Ta_{0.5}Hf_{0.5}Nb_{0.5}Zr$ coating on 316L SS has chunky HA particles which

are more frequently observed. SEM images of third week's samples are given in the Figure 4.4. below.

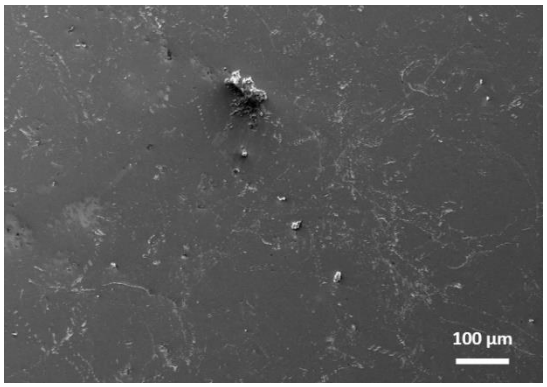

(a)

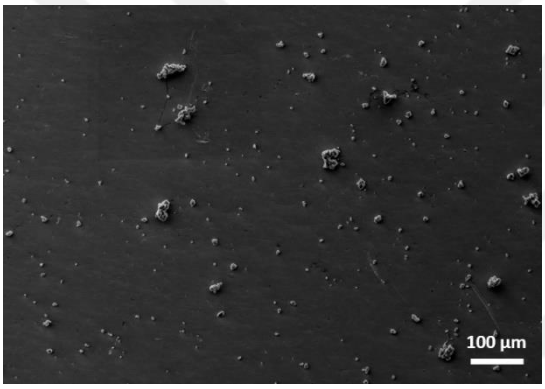

(b)

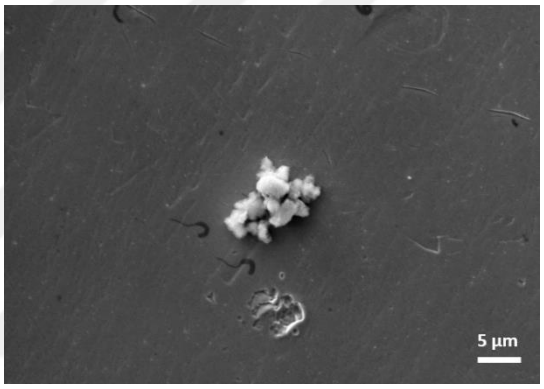

(c)

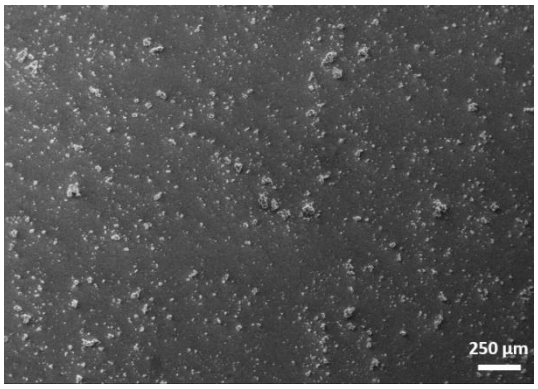

(d)

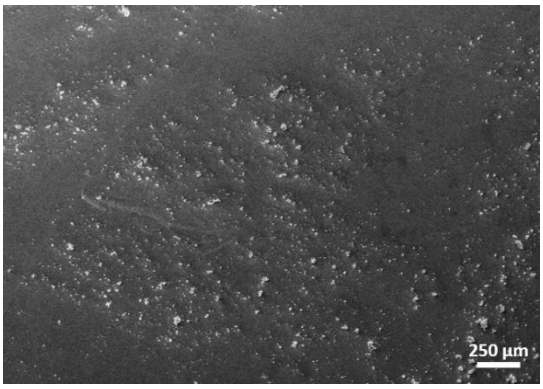

(e)

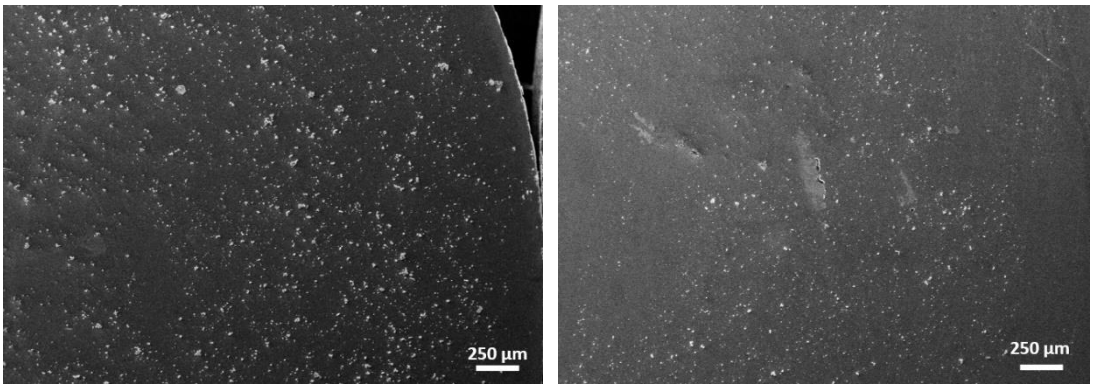

(f) **(g)**

Figure 4.4. After 3 weeks of immersion, SEM images taken from (a) 316 L stainless steel, (b) bulk TiTaHfNbZr, (c) bulk $Ti_{1.5}Ta_{0.5}Hf_{0.5}Nb_{0.5}Zr$, (d) TiTaHfNbZr coating on 316L SS, (e) oxidized TiTaHfNbZr coating on 316 L SS, (f) $Ti_{1.5}Ta_{0.5}Hf_{0.5}Nb_{0.5}Zr$ coating on 316L SS and (g) oxidized $Ti_{1.5}Ta_{0.5}Hf_{0.5}Nb_{0.5}Zr$ coating on 316L SS.

Figure 4.4. gives the SEM images of third week's samples. At the end of three weeks, all samples showed enhanced bioactivities compared to first week. However, HA dispersion is problematic on 316 L SS. There are separated HA particles in varying sizes. The biggest particle has 80 µm diameter. However, having chunky HA particles does not necessarily mean that a dense HA coating exists. HA nucleation sites must cover the whole surface homogeneously. Bulk TiTaHfNbZr possesses HA particles in diameters of 30 µm dispersed on the whole surface, which is a sign of very good HA coating. Bulk $Ti_{1.5}Ta_{0.5}Hf_{0.5}Nb_{0.5}Zr$ however, has no HA nucleation when it is compared to TiTaHfNbZr bulk. Only couple of nucleation with diameters of 2-5 µm exist. Probably the reason is that the sample was accidentally dropped to the table before it was put on the SEM sample holder. That might tear loosely bound HA particles off the surface. HEA coatings in fact have even better nucleation formation ability than bulk TiTaHfNbZr. 316L coated with 1 µm TiTaHfNbZr has the biggest particles, their diameters are generally around 30-40 µm but some of them even reaches to 90 µm. A crucial observation was made after Figures 4.4. (d) and(e) and Figures (f) and (g) were compared. Oxidation affected the bioactivity inversely. HA articles are smaller in size and there are less nucleation sites throughout the surfaces of oxidized HEA coatings. Thermal oxidation at 300 C^o air atmosphere for 5 minutes might change the surface morphology by coarsening the grains. Since oxidation acts as

annealing, some elements of HEA coatings might have been migrated to the surface forming metal oxides and this may also change the surface morphology leading to an inverse effect on HA nucleation.

SEM images of fifth week's samples are given in the Figure 4.5. below.

(a)

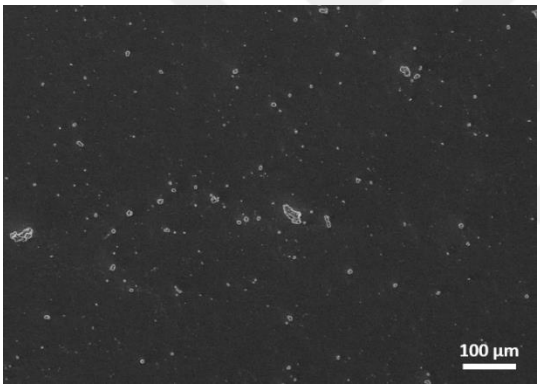

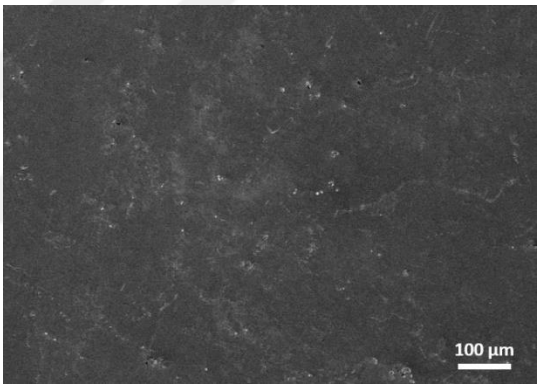

(b) **(c)**

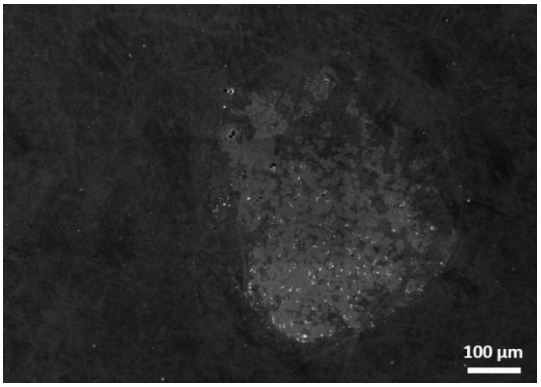

(d) **(e)**

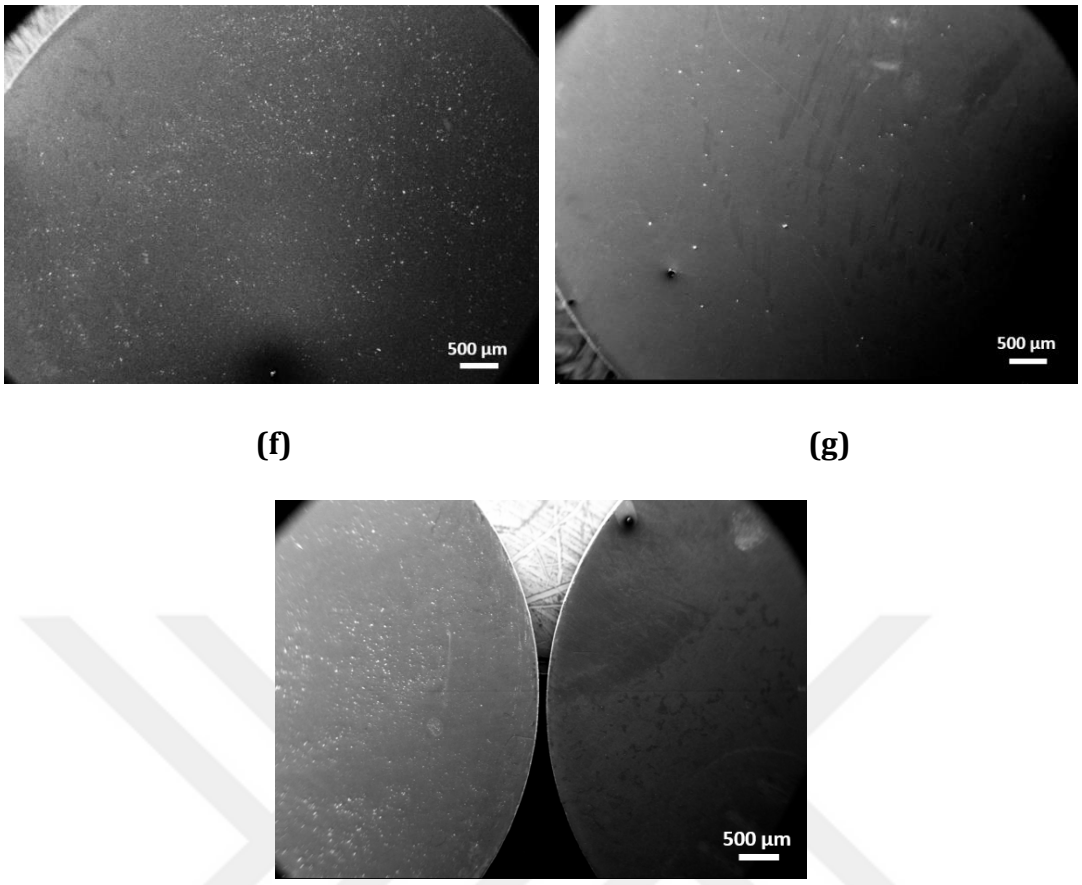

(f) **(g)**

(h)

Figure 4.5. After 5 weeks of immersion, SEM images taken from (a) 316 L stainless steel, (b) bulk TiTaHfNbZr, (c) bulk $Ti_{1.5}Ta_{0.5}Hf_{0.5}Nb_{0.5}Zr$, (d) TiTaHfNbZr coating on 316L SS, (e) oxidized TiTaHfNbZr coating on 316 L SS, (f) $Ti_{1.5}Ta_{0.5}Hf_{0.5}Nb_{0.5}Zr$ coating on 316L SS and (g) oxidized $Ti_{1.5}Ta_{0.5}Hf_{0.5}Nb_{0.5}Zr$ coating on 316L SS. And (h) a comparison of TiTaHfNbZr coating on 316L SS and oxidized TiTaHfNbZr coating on 316L SS. The sample on the right side is oxidized TiTaHfNbZr coating.

In the fifth week's SEM images, Figure 4.5. (a) shows HA nucleation on the margins of uncoated 316L SS. Throughout the whole surface, there are not many nucleation in fact, central region is rather empty. Especially after 5 weeks of immersion, bioactivity of commercial 316 L SS is still insufficient. Bulk HEAs possess many HA particles in varying sizes as they did in third week's samples. HA nucleation on bulk $Ti_{1.5}Ta_{0.5}Hf_{0.5}Nb_{0.5}Zr$ seem darker. This is probably because they are thinner than regular particles or nucleated chunky particles were fallen off from the surface leaving some traces behind. It is also

possible that thin and small HA particles might dissolve back to the surrounding environment [3]. However, even these traces are enough to make a comment on the high bioactivity of $Ti_{1.5}Ta_{0.5}Hf_{0.5}Nb_{0.5}Zr$. This supports the explanation of Figure 4.4. (c) saying the reason for the absence of HA particles is dropping the sample. Also, the number of nucleation is not as high as the bulk TiTaHfNbZr. Surface of TiTaHfNbZr coating is full of HA nucleation. They are dispersed homogeneously, and their sizes range from 2 to 45 μm. Oxidation of TiTaHfNbZr coating again decreased the bioactivity. In Figure 4.5. (e), there are salt particles and HA nucleation with 3 μm diameters accumulated in one region. Sample's surface seems stained on this region, this might be resulted from organic compounds. Even they are smaller, there are other HA particles too, but rest of the surface is rather empty compared to non-oxidized TiTaHfNbZr. Despite it is not exactly as good as TiTaHfNbZr coating, $Ti_{1.5}Ta_{0.5}Hf_{0.5}Nb_{0.5}Zr$ coating also has many HA nucleation. Maximum diameter of these nucleation is 35 μm and minimum is 2 μm. The difference between oxidized and non-oxidized coating is again easily seen on Figures 4.5. (f) and (g). Figure 4.5. (h) supplies a better comparison, the sample on the left is non-oxidized TiTaHfNbZr coating. Possible reasons for that was given in the above paragraph.

SEM images of seventh week's samples are given in the Figure 4.6. below.

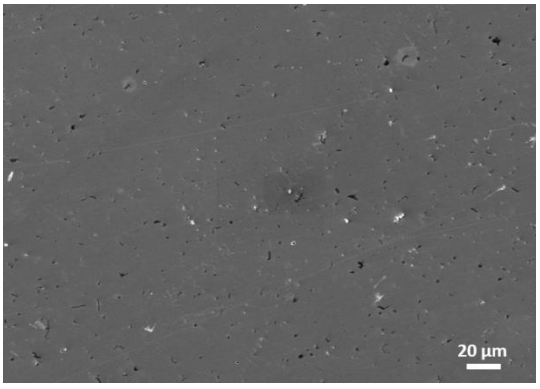

(a)

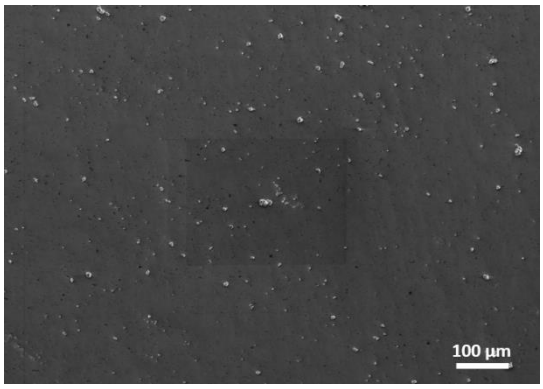

(b)

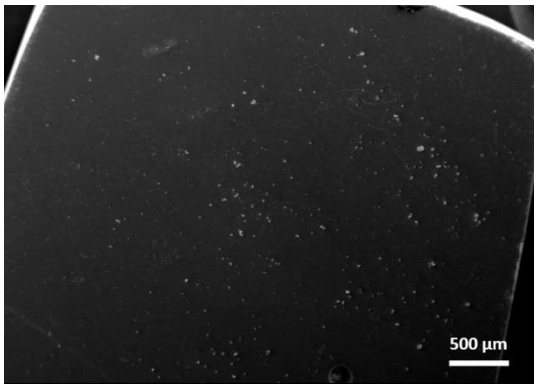

(c)

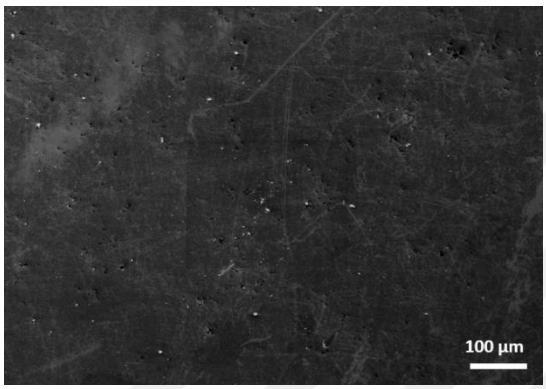

(d)

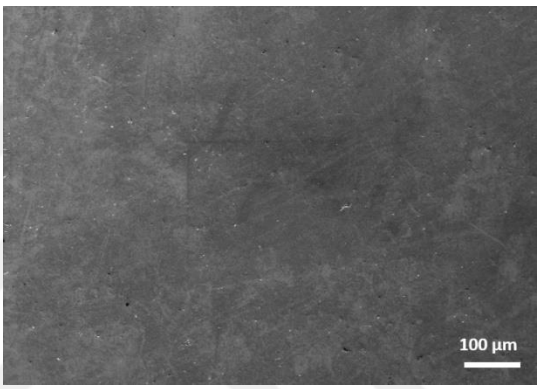

(e)

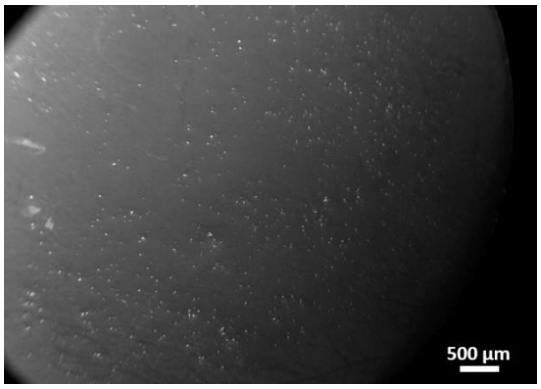

(f)

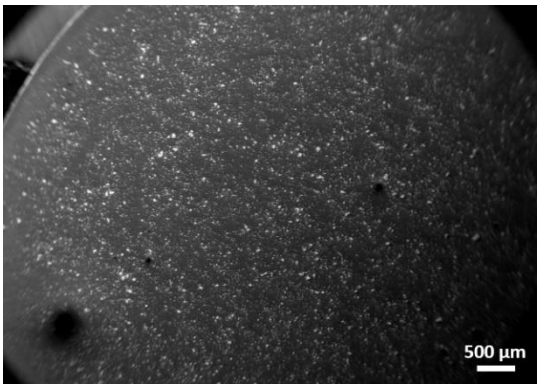

(g)

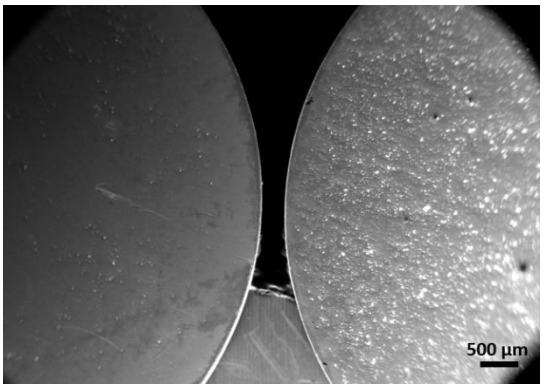

(h)

Figure 4.6. After 7 weeks of immersion, SEM images taken from (a) 316 L stainless steel, (b) bulk TiTaHfNbZr, (c) bulk $Ti_{1.5}Ta_{0.5}Hf_{0.5}Nb_{0.5}Zr$, (d) TiTaHfNbZr coating on 316L SS, (e) oxidized TiTaHfNbZr coating on 316 L SS, (f) $Ti_{1.5}Ta_{0.5}Hf_{0.5}Nb_{0.5}Zr$ coating on 316L SS and (g) oxidized $Ti_{1.5}Ta_{0.5}Hf_{0.5}Nb_{0.5}Zr$ coating on 316L SS. And (h) a comparison of TiTaHfNbZr coating on 316L SS and oxidized TiTaHfNbZr coating on 316L SS. The sample on the right side is oxidized TiTaHfNbZr coating.

Figure 4.6. (a) shows that even 7 weeks is not enough for 316L SS to show the same bioactivity that HEA coatings provided in 3 weeks. Wide-spread but very small HA particles cannot be regarded as a HA coating. Bioactivities of bulk HEAs are slightly increased, this is apparent from the HA particles having diameters up to 20 µm for TiTaHfNbZr and 60 µm for $Ti_{1.5}Ta_{0.5}Hf_{0.5}Nb_{0.5}Zr$ evenly dispersed throughout the surfaces. There is an unexpected situation on TiTaHfNbZr and oxidized TiTaHfNbZr coatings as can be seen in Figure 4.6. (d) and (e). Even though they are small and not many, there are HA particles on TiTaHfNbZr and bioactivity is similar to 316 L SS. Yet, oxidation decreased the bioactivity even more. The reason for that is probably not due to coating or the substrate, but due to complications during immersion, rinsing or SEM analysis. Otherwise, bioactivity of the HEA coatings would not be this perfect in the other samples, this samples are most likely exceptions. This is also proved in the Figure 4.6. (f) and (g). Even though there is a slight decrease in the bioactivity of $Ti_{1.5}Ta_{0.5}Hf_{0.5}Nb_{0.5}Zr$ coating comparing fifth week, HA particles are dispersed throughout the whole surface. Particles' diameters reach to 50 µm. After oxidation, the best HA coating seen in all seven weeks is observed. Particles with 2 to 70 µm diameters lay on the surface, there is a dense HA coating. The

effect of oxidation is more clearly seen in Figure 4.6. (h), the sample on the left is non-oxidized $Ti_{1.5}Ta_{0.5}Hf_{0.5}Nb_{0.5}Zr$ coating.

EDS analysis result of a typical HA particle is given in the Figure 7 below. Sample is 1µm TiTaHfNbZr coating on 316L SS after 1 week of immersion. Even though the sample surfaces are clean, there are some impurities such as dendritic NaCl particles, silica-based dirt, calcium based particles such as CaOC, organic compounds, carbon based dirt and oxides. Also, there are dents and scratches due to machining, grinding and sample handling with tweezers.

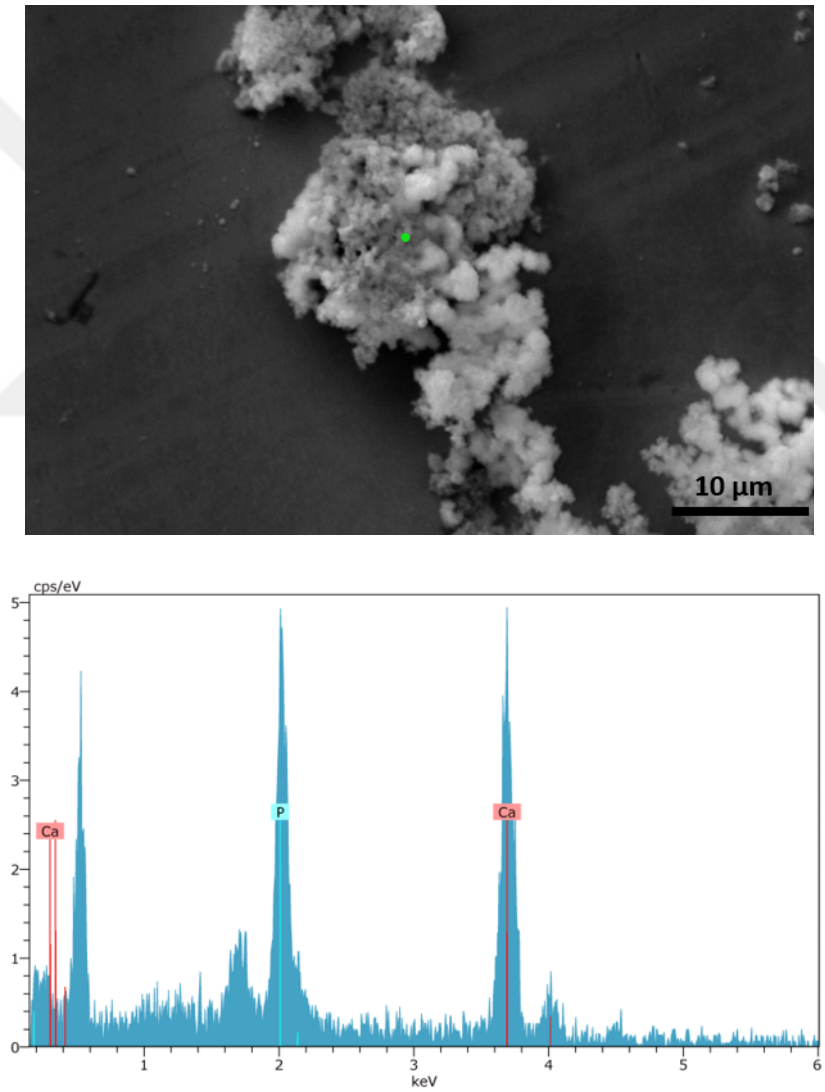

Figure 4.7. EDS analysis result of a typical HA particle nucleated on a 1µm TiTaHfNbZr coating on 316L SS after 1 week of immersion.

HEA coatings on 316 L substrate obviously increased HA nucleation. Sizes, intensities and numbers of the HA particles increased. HA tends to start its nucleation on the margins of samples. The bioactivity difference between 316L SS and HEA coatings and bulk HEAs pronounced even more with increasing immersion duration. Oxidation of HEA coatings decreased HA nucleation ability except 7 weeks immersed $Ti_{1.5}Ta_{0.5}Hf_{0.5}Nb_{0.5}Zr$ coating. TiTaHfNbZr coating and bulk showed better bioactivity than $Ti_{1.5}Ta_{0.5}Hf_{0.5}Nb_{0.5}Zr$ coating and bulk in 3rd and 5th weeks. In general, HEA coatings are better than HEA bulks. Bulk HEAs are crystalline, thus their surfaces are more rough than amorphous HEA coatings. Thermal oxidation acts as heat treatment and increases roughness of the surface because it favors crystallization [3]. The best HA formations were observed usually on non-oxidized amorphous HEA coatings. So, smooth surfaces might tend to supply better conditions for HA nuclei to reside on. However, the XRD peaks and AFM images following oxidation are needed to make solid comments. The improved bioactivity of oxidized $Ti_{1.5}Ta_{0.5}Hf_{0.5}Nb_{0.5}Zr$ coating after 7 weeks of immersion might be attributed to possible TiO_2 and ZrO_2 formations on the surface of HEA coating after thermal oxidation. These two oxides are generally used as adhesion layers for hydroxyapatite coatings in the earlier studies [3]. However, to explain the reason of not having the same effect in other oxidized coatings needs extra study.

SEM and EDS analyses of first week's 316 L SS and bulk HEA samples were conducted with ZEISS Ultra Plus Scanning Electron Microscope. The remaining samples were examined with ZEISS EVO LS 15 Scanning Electron Microscope. Bulk $Ti_{1.5}Ta_{0.5}Hf_{0.5}Nb_{0.5}Zr$ HEA's surfaces seem to have white points in third and fifth weeks. They are not nucleation or dirt. First week's bulk $Ti_{1.5}Ta_{0.5}Hf_{0.5}Nb_{0.5}Zr$ HEA does not show these dots. The reason for this might be the change of SEM device.

To evaluate the biocompatibility of HEA coatings, the ion releases from the samples are given in the Table 4.5 below and interpreted.

Table 4.5. Ni ion releases from samples to c-SBF in ppb. Bold values indicate higher ion release from coatings than that week's uncoated 316L SS.

Sample Name	Immersion Duration	Ni ion release (ppb)
TiTaHfNbZr bulk	1 week	2,11461
$Ti_{1.5}Ta_{0.5}Hf_{0.5}Nb_{0.5}Zr$ bulk	1 week	1,42977
TiTaHfNbZr coated 316L SS	1 week	3,25999
TiTaHfNbZr coated and oxidized 316L SS	1 week	2,84671
$Ti_{1.5}Ta_{0.5}Hf_{0.5}Nb_{0.5}Zr$ coated 316L SS	1 week	4,21041
$Ti_{1.5}Ta_{0.5}Hf_{0.5}Nb_{0.5}Zr$ coated and oxidized 316L SS	1 week	2,42162
316L SS	1 week	3,18902
TiTaHfNbZr bulk	3 weeks	1,55971
$Ti_{1.5}Ta_{0.5}Hf_{0.5}Nb_{0.5}Zr$ bulk	3 weeks	2,16187
TiTaHfNbZr coated 316L SS	3 weeks	1,99072
TiTaHfNbZr coated and oxidized 316L SS	3 weeks	2,84664
$Ti_{1.5}Ta_{0.5}Hf_{0.5}Nb_{0.5}Zr$ coated 316L SS	3 weeks	9,65973
$Ti_{1.5}Ta_{0.5}Hf_{0.5}Nb_{0.5}Zr$ coated and oxidized 316L SS	3 weeks	3,78822
316L SS	3 weeks	4,8481
TiTaHfNbZr bulk	5 weeks	1,72494
$Ti_{1.5}Ta_{0.5}Hf_{0.5}Nb_{0.5}Zr$ bulk	5 weeks	1,73087
TiTaHfNbZr coated 316L SS	5 weeks	4,61785

TiTaHfNbZr coated and oxidized 316L SS	5 weeks	4,55966
$Ti_{1.5}Ta_{0.5}Hf_{0.5}Nb_{0.5}Zr$ coated 316L SS	5 weeks	7,0106
$Ti_{1.5}Ta_{0.5}Hf_{0.5}Nb_{0.5}Zr$ coated and oxidized 316L SS	5 weeks	6,40835
316L SS	5 weeks	3,4649
TiTaHfNbZr bulk	7 weeks	1,11697
$Ti_{1.5}Ta_{0.5}Hf_{0.5}Nb_{0.5}Zr$ bulk	7 weeks	1,53014
TiTaHfNbZr coated 316L SS	7 weeks	6,80822
TiTaHfNbZr coated and oxidized 316L SS	7 weeks	5,718
$Ti_{1.5}Ta_{0.5}Hf_{0.5}Nb_{0.5}Zr$ coated 316L SS	7 weeks	8,61521
$Ti_{1.5}Ta_{0.5}Hf_{0.5}Nb_{0.5}Zr$ coated and oxidized 316L SS	7 weeks	2,10273
316L SS	7 weeks	3,38278

According to the data provided in Table 4.5, bulk HEAs released less ions than 316L SS in all weeks. In fact, there is no release from bulk HEAs because they are 99.99 % pure. The release readings attained from bulk HEAs are due to Ni impurities of chemicals used in SBF preparation. In one week immersed samples, ion releases from non-oxidized HEA coatings were more than uncoated 316L SS. However, thermal oxidation supplied an effective protection against Ni ion leakage from 316L SS substrate and release amounts are less than uncoated 316L SS. This might be due to metal oxides formed on the surface of HEA coating, filling microcracks between the grains. Since the annealing results in grain coarsening as previously mentioned, the microcracks must have been widened even more. Even though this should have increased the release, an opposite situation occurred. Hence metal oxides are widely used as protective layers against toxic effects of substrate materials, this assumption is made [24,25]. After 3 weeks of immersion, oxidized and non-oxidized TiTaHfNbZr coatings effectively protected the SBF in a great extent. So that release from these coatings are close to that from bulk HEAs. $Ti_{1.5}Ta_{0.5}Hf_{0.5}Nb_{0.5}Zr$ coated 316L SS however, destroyed ion leakage shielding causing twice as much ion release from

uncoated 316L SS. Yet, thermal oxidation again fixed this problem as in the first week. In the 5 weeks immersion sample set, all coatings failed to supply ion release barrier. This is probably because discontinuous coatings due to cracks, scratches, voids and broken off regions. Examples of broken off and scratched coatings observed on SEM images of 5th week's coatings are given in the Figure 4.8. below:

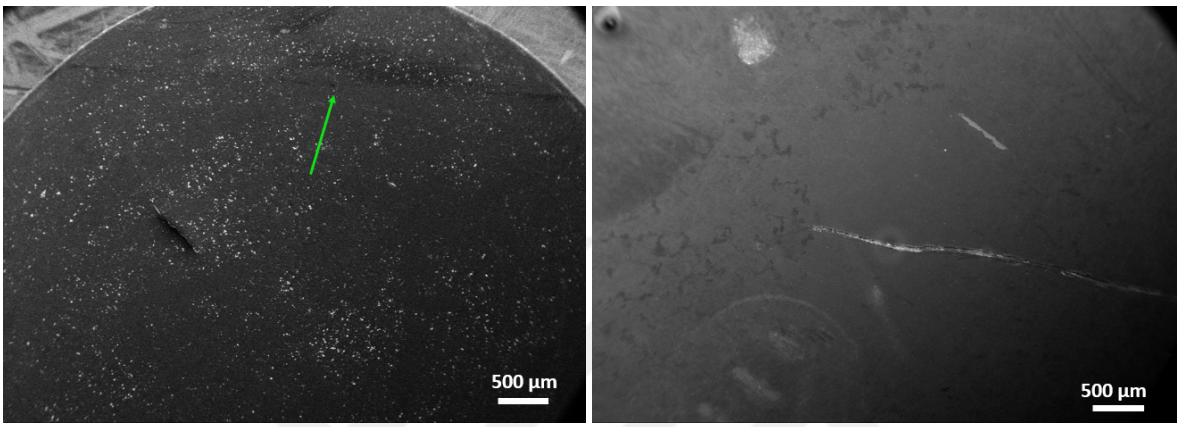

(a) **(b)**

Figure 4.8. (a) Break off observed on the upper region of TiTaHfNbZr coating on 316L SS after 5 weeks of immersion. Green arrow shows the position of break off. This region is even visible to eye appearing darker than other regions. (b) The several millimeters long scratch on the oxidized TiTaHfNbZr coating on 316L SS after 5 weeks of immersion.

The only effective coating among 7th week's samples is oxidized $Ti_{1.5}Ta_{0.5}Hf_{0.5}Nb_{0.5}Zr$ coating. Ion release from remaining coatings are 2-3 times that of uncoated 316 L SS. Among failed coatings, oxidized TiTaHfNbZr is the best one. That means oxidized coatings again proved to have better biocompatibility than as deposited ones. Figure 4.9. below shows the broken off region on TiTaHfNbZr coating.

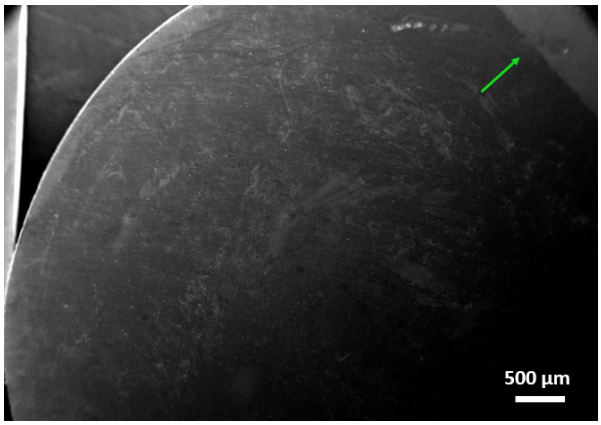

Figure 4.9. Break off observed on the upper region of TiTaHfNbZr coating on 316L SS after 7 weeks of immersion. Green arrow shows the position of break off. This region is even visible to eye appearing darker than other regions.

The HEA coated samples which caused high amounts of Ni ion release are subjected to XPS analysis on Thermo K-Alpha X-ray Photoelectron Spectrometer. Readings are taken from a circular region with 400 µm of diameter, 10 nm deep from the surface. All readings showed Fe 3p peaks indicating these regions are not coated, 316L SS is directly in contact with SBF. Figure 4.10. below shows the XPS date taken from TiTaHfNbZr coating on 316L SS, immersed for 7 weeks.

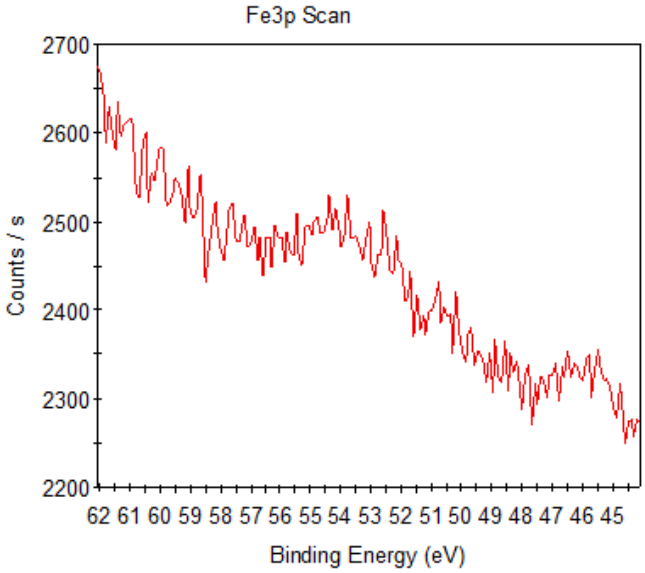

Figure 4.10. XPS results showing Fe 3p counts taken from TiTaHfNbZr coating on 316L SS, immersed for 7 weeks.

It is observed that cumulative Ni ion releases from samples fluctuates upon 7 weeks of immersion. The trend of this fluctuation is provided on a graph in Figure 4.11. below.

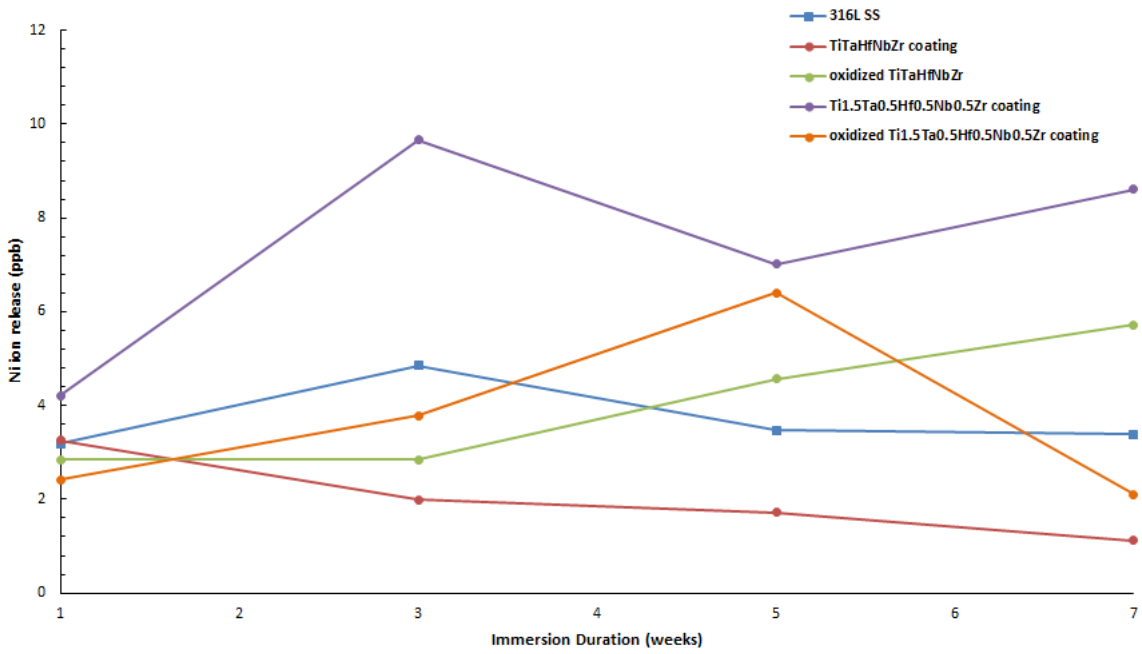

Figure 4.11. Fluctuating cumulative Ni ion releases from samples upon 7 weeks.

These trends are not reasonable assuming that all coatings and all substrates are perfectly identical. The ion release rates can fluctuate due to protective layer formation and dissolution between different immersion durations as other studies revealed, but the cumulative ion releases should increase or at least stay constant [25]. The reason for these unbalanced trends is possibly the different coating qualities because all samples are immersed in same SBF solutions, stored and analyzed altogether. The high amounts of Ni ion releases from erroneously coated samples show that HEA coating is a risky surface modification method. If it is not properly done, results are catastrophic. Such massive amount of ion releases generally stems from pitting corrosion rather than a uniform corrosion. Pitting corrosion causes due to small crevices on the surface. When these small

cavities are deaerated, local anode and cathode regions form on the surface. Inside of the crevice acts as anode while the circumference of the crevice borders acts as cathode. An anodic current starts to flow in between these locations, oxidation starts inside the cavities. Metal ions that released due to oxidation travels outside of the pits, they are reduced and nucleated as metal oxides [11,24,26]. In the currents study, the Mn content in 316L SS decreases the alloy's resistance to pitting corrosion in Cl^- rich solution such as the SBF [14]. During SEM analyses, oxide formations were observed many times, they might be indicators of pitting corrosion, yet further analyses are needed. One of the proposed precautions to pitting corrosion is amorphous film coating [24,27]. However, if this coating is not uniform and dense, discontinuities might act as crevices indeed, increasing the risk of ion release. During ICP-MS analyses, Cr ion release was also measured but since most of the samples did not show any release, Ni ion release is focused.

Conclusion

This study reveals that PVD coating of 1µm thick TiTaHfNbZr and $Ti_{1.5}Ta_{0.5}Hf_{0.5}Nb_{0.5}Zr$ coatings improves the hardness of 316L stainless steels without sacrificing from elastic modulus. As deposited HEA coatings provide outstanding enhancement on the bioactivity of 316L stainless steel, thermally oxidized coatings also showed very good bioactivity. Especially thermally oxidized HEA coatings are promising barriers to toxic ion release. However, continuity and density of the coating is crucial to avoid catastrophic ion release. Together with excellent mechanical properties and hydroxyapatite formation ability, HEA coated 316L stainless steels are suitable for load-bearing orthopedic implants. Yet, their biocompatibility needs improvements and extra effort.

Bibliography

1. Ducheyne, P. (Ed.), *Comprehensive Biomaterials*. (Elsevier, 2011).

2. Pradeep, K., Kumar, P., Duraipandy, N., Manikantan Syamala, K. & Rajendran, N. Antibacterial effects, biocompatibility and electrochemical behavior of zinc incorporated niobium oxide coating on 316L SS for biomedical applications. *Appl. Surf. Sci.* **427,** 1166–1181 (2018).

3. Driver, M. (Ed), *Coatings for biomedical applications* (Woodhead Publishing Limited, Cambridge, 2012).

4. Motallebzadeh, A., Yagci, M. B., Bedir, E., Aksoy, C. B. & Canadinc, D. Mechanical Properties of TiTaHfNbZr High-Entropy Alloy Coatings Deposited on NiTi Shape Memory Alloy Substrates. *Metall. Mater. Trans. A Phys. Metall. Mater. Sci.* **49,** 1992–1997 (2018).

5. Murty, B. S., Yeh, J. W. & Ranganathan, S. *High Entropy Alloys.* (Elsevier, 2014).

6. Tsai, M.-H. & Yeh, J.-W. High-Entropy Alloys: A Critical Review. *Mater. Res. Lett.* **2,** 107–123 (2014).

7. Tüten, N., Canadinc, D., Motallebzadeh, A. & Bal, B. Microstructure and tribological properties of TiTaHfNbZr high entropy alloy coatings deposited on Ti–6Al–4V substrates. *Intermetallics* **105,** 99–106 (2019).

8. Basu, B., Katti, D. S. & Kumar, A. *Advanced Biomaterials: Fundamentals, Processing, and Applications*. (John Wiley & Sons, INC , 2009).

9. Lu, Z. P. *et al.* An assessment on the future development of high-entropy alloys: Summary from a recent workshop. *Intermetallics* **66,** 67–76 (2015).

10. Tsai, K.-Y., Tsai, M.-H. & Yeh, J.-W. Sluggish diffusion in Co–Cr–Fe–Mn–Ni high-entropy alloys. *Acta Mater.* **61,** 4887–4897 (2013).

11. Yaszemski, M., Trantolo, D. J., Lewandrowski, K., Hasirci, V., Altobelli, D. E. Wise, D. L. *Biomaterials in Orthopedics* (2004).

12. Yang, X. & Zhang, Y. Prediction of high-entropy stabilized solid-solution in multi-component alloys. *Mater. Chem. Phys.* **132,** 233–238 (2012).

13. Wang, X. F., Zhang, Y., Qiao, Y. & Chen, G. L. Novel microstructure and properties of multicomponent CoCrCuFeNiTix alloys. *Intermetallics* **15,** 357–362 (2007).

14. Gao, M. C., Liaw, P. K., Yeh, J. W. & Zhang, Y. (Eds.) *High-Entropy Alloys: Fundamentals and Applications* (Springer, 2016).

15. Xing, Q. W. & Zhang, Y. Amorphous phase formation rules in high-entropy alloys. *Chinese Phys. B* **26,** (2017).

16. Inoue, A. Stabilization of metallic supercooled liquid and bulk amorphous alloys. *Acta Mater.* **48,** 279–306 (2000).

17. Slater, J. C. Atomic radii in crystals. *J. Chem. Phys.* **41,** 3199–3204 (1964).

18. Clementi, E., Raimondi, D. L. & Reinhardt, W. P. Atomic screening constants from SCF functions. II. Atoms with 37 to 86 electrons. *J. Chem. Phys.* **47,** 1300–1307 (1967).

19. Yeh, J.-W. Recent Progress in High-entropy Alloys. *European Journal of Control.* **31** (6)**,** 633–648 (2006).

20. Tsau, C. H., Hwang, Z. Y. & Chen, S. K. The Microstructures and Electrical Resistivity of (Al, Cr, Ti)FeCoNiO<inf>x</inf> High-Entropy Alloy Oxide Thin Films. *Adv. Mater. Sci. Eng.* 2015, (2015).

21. Li, X., Zheng, Z., Dou, D. & Li, J. Microstructure and Properties of Coating of FeAlCuCrCoMn High Entropy Alloy Deposited by Direct Current Magnetron Sputtering. *Mater. Res.* **19,** 802–806 (2016).

22. Wang, H. *et al.* Structure, corrosion resistance and in vitro bioactivity of Ca and P containing TiO 2 coating fabricated on NiTi alloy by plasma electrolytic oxidation. *Appl. Surf. Sci.* **356,** 1234–1243 (2015).

23. Asanithi, P. Surface porosity and roughness of micrographite film for nucleation of hydroxyapatite. *J. Biomed. Mater. Res. - Part A* **102,** 2590–2599 (2014).

24. Tan, L., Dodd, R. A. & Crone, W. C. Corrosion and wear-corrosion behavior of NiTi modified by plasma source ion implantation. *Biomaterials* **24,** 3931–3939 (2003).

25. Uzer, B., Birer, O. & Canadinc, D. Investigation of the Dissolution–Reformation Cycle of the Passive Oxide Layer on NiTi Orthodontic Archwires. *Shape Mem. Superelasticity* (2017).

26. Bassey, I. Recent Advances in Computational Design of Organic Materials for Corrosion Protection of Steel in Aqueous Media. *Dev. Corros. Prot.* (2014).

27. Sui, J. H. & Cai, W. Effect of diamond-like carbon (DLC) on the properties of the NiTi alloys. **15,** 1720–1726 (2006).

CHAPTER 5. CONCLUSION AND FUTURE WORK

This study investigates PVD coatings of TiTaHfNbZr and $Ti_{1.5}Ta_{0.5}Hf_{0.5}Nb_{0.5}Zr$ on NiTi and 316L stainless steel substrates. Mechanical performances, microstructures, bioactivity and biocompatibility of coatings were analyzed using various methods such as nanoindentation, XRD, AFM, SEM, EDS, XPS and ICP-MS. Results proved that HEA coating is a promising surface modification method since it provides improvements on mechanical properties, bioactivities and biocompatibilities of the metallic substrates that they deposited on. Effect of oxidation on XRD patterns, surface roughness and mechanical properties of HEA coatings deposited on 316L stainless steels needs further analyses. *In-vitro* cell culture tests should also be conducted for NiTi substrates. HEA coated 316L stainless steel and NiTi SMA samples must be examined in pitting tests. Also, methods to control and reduce the internal stress of the films during deposition process should be studied. Also, computer programs can be used for making computational analyses on the elemental distribution of HEA coatings and bulks prior to production. These programs supply consistent predictions on the alloy's mechanical properties and corrosion resistances. Cell culture and viability experiments are necessary to make the most accurate interpretations on bioactivity and biocompatibility of HEA coatings.